

Introduction:

Venus, the most Earth-like planet in size and mass, experienced a very different history than Earth. Venus' thick atmosphere of carbon dioxide, seventy times more dense than that of the Earth, hides her surface from optical view.

Venus, an extremely dry planet, contains almost no water. Venus' hot surface, approximately 750K, exhibits globally distributed volcanic and tectonic features, yet it records no evidence of plate tectonic processes and little evidence of extensive erosion. Instead of Earth's linear belts, Venus hosts many circular to quasi-circular structures ranging from about 1 to 2600 km in diameter.

The largest circular structures, approximately 1400 to 2600 km, consist of volcanic rises and crustal plateaus. Dome-like topographic swells define volcanic rises, whereas, steep-sided flat-topped structures characterize crustal plateaus (Phillips and Hansen, 1994; Smrekar et al., 1997). Other circular structures, chiefly impact craters and coronae, decorate the surface of Venus. Impact craters are circular depressions surrounded by a rim ranging from about 1.5 to 270 km in diameter caused by an exogenic process (Phillips et al., 1992, Schaber et al., 1992).

A suite of approximately 515 circular to quasi-circular structures, called coronae, with diameters ranging from approximately 60 to 2600 km, overlap the range of diameters seen in volcanic rises, crustal plateaus, and impact craters (Stofan et al., 1992). Coronae, which are characterized by an annulus of fractures or ridges, variably display radial fractures, lava flows, and double ring structures (Barsukov et al., 1986; Basilevsky et al., 1986; Pronin and Stofan,

1990; Stofan et al., 1992; Stofan et al., 1997). Interpreted as the result of both exogenic and endogenic processes, coronae are variably interpreted to have formed by bolide impacts, collapsed calderas, and lithosphere diapiric structures (Basilevsky et al., 1986; Stofan and Head, 1990; Stofan et al., 1991; Janes et al., 1992; Stofan et al., 1992; Squyres et al., 1992; Koch, 1994; Cyr and Melosh, 1993; Koch and Manga, 1996; Vita-Finzi et al., 2004; Hamilton, 2004), although most workers favor diapiric mechanisms.

The wide range of corona characteristics suggests that coronae may form by more than one process. In this contribution I examine a specific morphological subset of coronae, those marked by circular amphitheater-like depressions. I call these features circular lows in order to highlight them as a subset of coronae, based on their features rather than the mode of formation. I constructed detailed geologic maps of five individual circular lows using NASA Magellan synthetic aperture radar (SAR) and altimetry data. The geologic maps and interpreted geologic histories are not easily reconciled with either a diapiric mode of formation or with caldera collapse. The distinctive features of circular lows appear to be more consistent with characteristics used to define impact craters. If circular lows are ancient impact craters, then Venus' average model surface age and local histories may be older than currently appreciated.

Background:

In 1990-1994 the Magellan mission mapped 98 percent of Venus' surface producing a dataset of approximately 100 m radar resolution (Ford and Plaut, 1993; Saunders et al., 1992). Actual spatial resolution varied with latitude. The Magellan mission allowed high-resolution global characterization of landforms and tectonic features, and it provided data for use in studying surface and interior processes (Ford, 1993).

Venus preserves approximately 970 pristine impact craters, distributed in near random fashion across the planet (Phillips et al., 1992; Schaber et al., 1992, Herrick et al., 1997). General characteristics of Venus' impact craters include 1) circular depressions, 2) diameters ranging from approximately 1.5 to 270 km, 3) rims surrounding central depressions, and 4) ejecta deposits adjacent to the rim (Schaber et al., 1992, Herrick and Phillips, 1994; Herrick and Sharpton, 1996, McKinnon et al., 1997). Some craters have halos, radar smooth areas that surround the impact crater; other impact crater characteristics depend on crater diameter. Impact craters with diameters greater than 45 km may have central peaks on the crater's basin floor and may display a double ring surrounding the basin (Hartmann, 1999). Craters with diameters greater than 100 km may exhibit multiple concentric rings. The innermost ring may be roughly circular and partially flooded with lava that covers the basin floor; the outer ring may consist of a ring or a well-defined crest, typical of structures associated with ordinary impact craters (Hartmann, 1999). Mead, the largest recognized impact crater

with a diameter of 269 km, hosts two concentric rings and a flooded interior (Fig. 1).

Approximately 515 coronae have been identified, ranging in diameter from approximately 60 to 2600 km, with a median of about 200 km (Stofan et al., 1992; Stofan et al., 1997; Stofan et al., 2001) (Fig. 2). Coronae occur in 1) chains associated with chasmata (troughs), 2) clusters associated with volcanic rises, and 3) as isolated features in the lowlands (Stofan et al., 1992; Jurdy and Stefanick, 1999; Smrekar and Stofan, 1999). Coronae host various tectonic and volcanic features. Tectonic features include concentric ridges, annuli of fractures and ridges, radial fractures and interior graben (Basilevsky et al., 1986; Stofan and Head, 1990; Stofan et al., 1991; Janes et al., 1992; Stofan et al., 1992; Squyres et al., 1992). Volcanic features include interior flow deposits, individual shields (2 to 20 km in diameter), small calderas (20 to 50 km across), collapsed pits, and exterior flows (Basilevsky et al., 1986; Stofan and Head, 1990; Stofan et al., 1991; Janes et al., 1992; Stofan et al., 1992; Squyres et al., 1992). Coronae topographic profiles (Fig. 3) range from domical to plateau-shaped, rimmed depressions, to amphitheater-like depression, to no topographic expression (Smrekar and Stofan, 1997; Stofan et al., 1997). The wide range of topographic profiles has been attributed to differing developmental stages of corona evolution (Smrekar and Stofan, 1997). Although some coronae have been interpreted as exogenic products (e.g. Schaber and Boyce, 1977; Campbell et al., 1979; Campbell and Burns, 1980; Jurgens et al., 1980; Marsursky et al., 1980; Grieve and Head, 1981; Head and Solomon, 1981; Barsukov et al., 1986; Nikolayeva et

al., 1986; Basilevsky, 1987; Squyres et al., 1992; Vita-Finzi, 2004; Hamilton, 2004), since the acquisition of Magellan high resolution SAR data most workers favor a diapiric origin (e.g. Janes et al., 1992; Squyres et al., 1992; Janes and Squyres, 1995; Stofan et al., 1997; Jurdy and Stefanick, 1999; Smrekar and Stofan, 1999; Hansen, 2003).

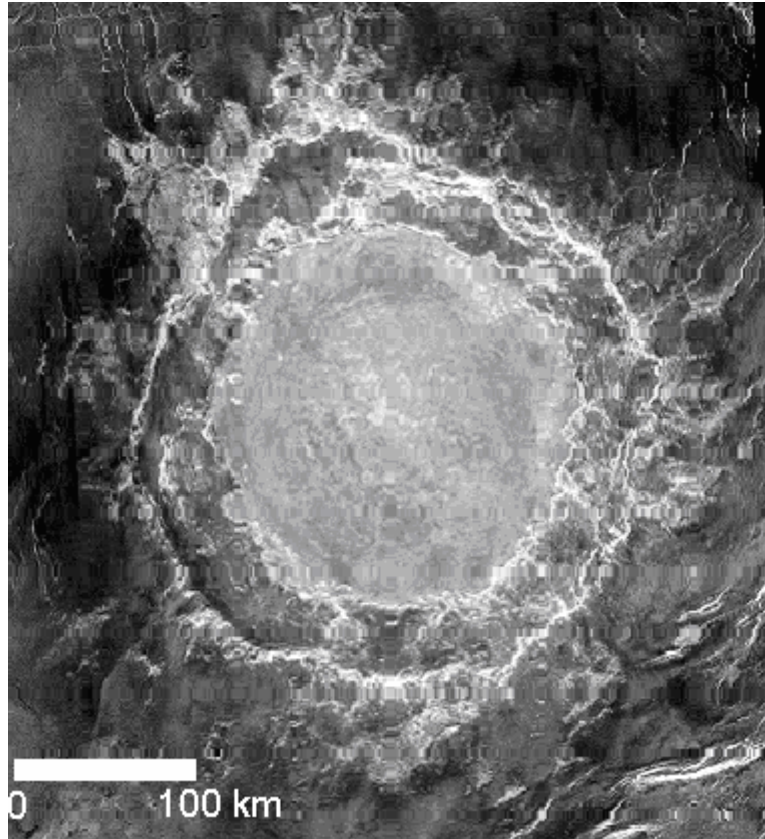


Figure 1. Left-illumination SAR image of Mead impact crater (12.50 N, 57.20 E) is the largest impact on Venus with a diameter of 269 km and 1 km depth. The bright patches covering and surrounding the rim are ejecta.

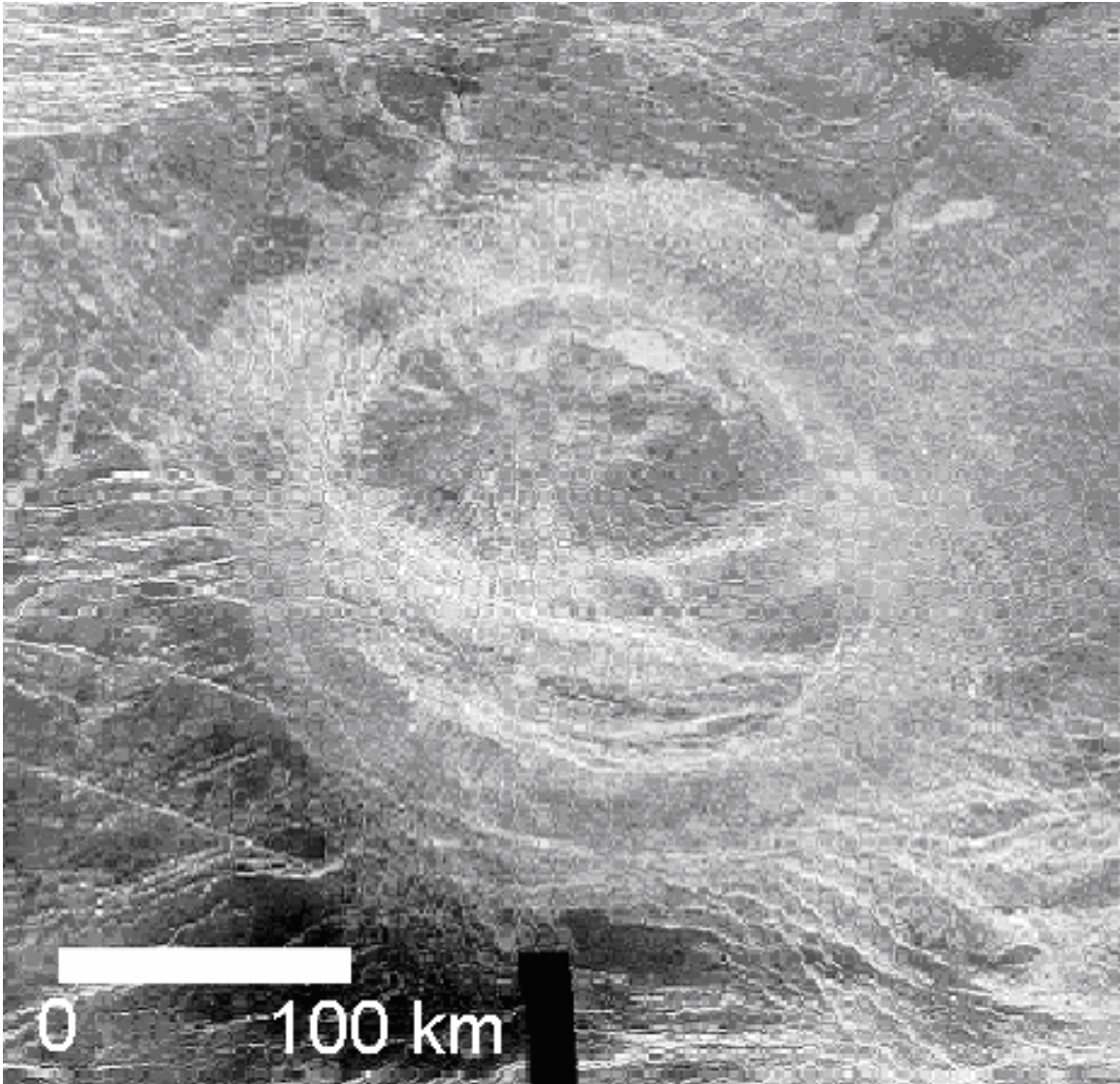


Figure 2. Left-illumination SAR image of Gashan-Ki Corona (11.7 N, 243.7 E), the corona has a diameter of 290 km (Stofan et al., 1992) with a concentric double ring of fractures. The central region has radial fractures fanning outward.

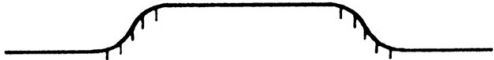
Group	Topographic profile	Description	% of coronae
1		Dome	10
2		Plateau	10
3a		Rim surrounding interior high	21 (a+b)
3b		Rim surrounding interior dome	
4		Rim surrounding depression	25
5		Outer rise, trough, rim, inner high	5
6		Outer rise, trough, rim, inner low	1
7		Rim only	7
8		Depression	7
9		No discernible signature	14

Figure 3. A cartoon of nine types of topographic profiles associated with coronae ranging from domical to plateau-shaped, rimmed depression, to amphitheater-like depression, to no topographic signature. (after Smerkar and Stofan, 1997)

Data:

The Magellan mission collected globally-extensive synthetic-aperture radar (SAR), altimetry, gravity, and emissivity data. Magellan's SAR system used an antenna attached to the satellite that emitted pulses towards the planet's surface. The antenna moved through a series of positions along its path as it was releasing and receiving pulses to create a radar image (Fig. 4). Altimetry is measured as distance from the planet center (Plaut, 1993). Scientists produced topographic maps of the surface by measuring the standard height, with mean planetary radius (MPR) as a datum (Plaut, 1993). Gravity data is most useful when used in combination with altimetry data. Gravity maps indicate density variations in a planet's interior (Ford and Plaut, 1993). Even at the highest gravity resolution, the available gravity data is too coarse to resolve the features (less than 400 km) mapped herein. Emissivity data represent a measure of how well an object approximates a perfect blackbody radiator; a good emitter needs to be a good absorber and a poor reflector (Plaut, 1993). My research used Magellan SAR and altimetry data sets.

The Magellan satellite conducted five global mapping cycles; cycle 1 collected left-illumination SAR, cycle 2 collected right-illumination SAR, cycle 3 collected left-illumination stereo SAR, and cycles four and five collected gravity data (Ford and Plaut, 1993). Cycles one through three also collected altimetry data at the same time as collecting the SAR data. Left-illumination and right-illumination made-up the SAR images based on the angles the satellite recorded the images from. I used left-illumination SAR images to map the circular lows, supplemented by right-illumination and stereo data where available. Cycles one

and three of SAR data can be combined to produce a red-blue anaglyph that mimics true stereo. Synthetic stereo combines SAR data and altimetry to make synthetic red-blue anaglyphs. (Refer to Appendix for more information)

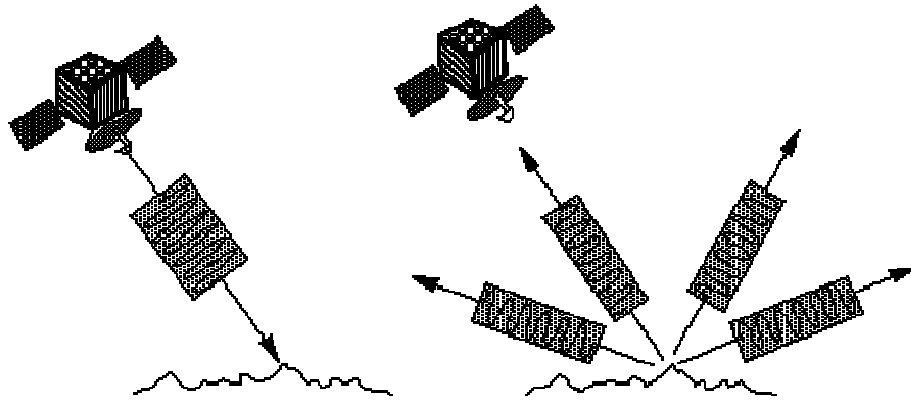


Figure 4. A cartoon of how a satellite radar system works. The antenna attached to the satellite sends out pulses towards the planet's surface. As the satellite moves along its path it receives the pulses it previously released. (After Freeman, 1996)

Methods:

I conducted a global survey, using SAR and altimetry data, to determine the location and number of circular lows on Venus. The characteristics I used to identify circular lows are: 1) circular structure, 2) amphitheater-like depression, 3) lack of radial fractures, and 4) possible rim. Approximately 50 circular lows were identified in the lowlands with diameters ranging from about 60 to 380 km (Table I). Using this survey, I then selected five specific circular lows to map in detail; four are located in areas of tessera terrain and one is adjacent to two domical coronae. The circular lows were selected based on character and data availability.

Full-resolution SAR data for each map area were obtained from the US Geological Survey (<http://pdsmaps.wr.usgs.gov/maps.html>). Where possible I used cycle 1, 2 and 3 data (Table II). All SAR images were viewed in both normal and inverted modes. Inverted modes were created using Adobe Photoshop™ image functions. Where data allowed, I constructed true stereo views by combining left-illumination SAR and stereo SAR in Adobe Photoshop™ (Plaut, 1993). In each case I also used synthetic stereo imagery (Kirk et al., 1993) constructed with macros developed by D.A. Young. Mapping was conducted digitally using Adobe Illustrator™; geological images were stretched and inverted using Adobe Photoshop™.

SAR and altimetry data were used to determine the diameter, depth and width of depression, the height of the circular low compared to its surrounding area, and the width of the annulus of concentric fractures (Fig. 5). Topographic

profiles of the circular lows illustrate the depth, width, and height of each depression, as well as the base elevation of the map (Fig. 5; Table III).

Primary and secondary structures provide clues to formation processes or material unit properties (Hansen, 2000). Primary structures include (Fig. 6): shield edifices, flows, channels, pit chains, and impact craters. Small, domical or cone-shaped volcanoes (less than 20 km) spaced closely together describe shields. Channels are at surface tubular passageways. Chains of small depressions (less than 20 km in diameter) portray pit chains. Secondary or tectonic structures form after the material unit deposition and therefore record processes that are different from the material unit and primary structures (Hansen, 2000). Secondary structures I mapped include (Fig. 7): ribbons, folds, graben, wrinkle ridges, and fractures. Ribbons fabrics represent alternating steep-sided ridges and troughs (Hansen and Willis, 1996; Hansen and Willis 1998). Blocks of crustal units bounded on either side by inward-dipping normal faults mark graben. Sinuous ridges with a positive topographic signature describe wrinkle ridges and lineaments with a negative topographic signature, or no discernable topographic signature describe fractures. Fracture suites occur in a variety of patterns, such as concentric, radial, and parallel (Fig. 7). Geologic maps of each circular low provide information to determine the geologic histories, which in turn provide clues to operative processes responsible for circular low formation.

Table I. Identified Circular Lows

<i>Latitude (degrees)</i>	<i>Longitude (degrees)</i>	<i>Quadrangle</i>	<i>Name</i>	<i>Diameter (km)</i>
38.3	18.8	V8 - Bereghinya Planitia	Cavell	100
37.5	67.5	V10 - Tellus Tessera	Olwen	175
26.5	94.5	V11 - Shimti Tessera	Eurynome	200
33	143	V12 - Vellamo Planitia	Ved-Ava	200
48.7	247	V16 - Kawelu Planitia	Nalwanga	380
28.5	243	V16 - Kawelu Planitia	Unknown	122.5
8.3	11.7	V20 - Sappho Patera	Sunrta	170
3	81.8	V22 - Hestia Rupes	Habonde	125
17	63.5	V22 - Hestia Rupes	Unknown	78.75
1.5	72	V22 - Hestia Rupes	Unknown	52
23	98	V23 - Niobe Planitia	Maya	225
16.5	119	V23 - Niobe Planitia	Omeciuatl	175
15	118	V23 - Niobe Planitia	Bhumiya	100
15.5	114	V23 - Niobe Planitia	Allatu	125
18.5	125	V24 - Greenway	Abundia	250
19.2	123.5	V24 - Greenway	Nintu	75
15.5	132.5	V24 - Greenway	Kubebe	125
19.5	153.5	V25 - Rusalka Planitia	Ituana	220
9.4	254.7	V28 - Hecate Chasma	Ak-Ene	150
14	258.8	V28 - Hecate Chasma	Nei-Teukez	90
14	302.5	V30 - Guinevere Planitia	Unknown	120
5	311	V30 - Guinevere Planitia	Unknown	131.25
7.5	313	V30 - Guinevere Planitia	Unknown	78.75
-6.5	12.9	V32 - Alpha Regio	Thouris	190
-5.5	19	V32 - Alpha Regio	Unknown	105
-7.5	34.5	V33 - Scapellini	Unknown	60
-5.5	65.2	V34 - Ix Chel Chasma	Verdandi	180
-7.5	118	V35 - Ovda Regio	Unknown	60
-12.5	327.5	V42 - Navaka Planitia	Katielo	210
-17.2	343.6	V43 - Carso	Bhumidevi	150
-36	21.8	V44 - Kaiwan Fluctus	Pachamama	130
-37	43	V45 - Agnesi	Xcanil	200
-33.5	50	V45 - Agnesi	Zemlika	150
-27.5	50.5	V45 - Agnesi	Umay-ene	370
-26.3	82	V46 - Aino Planitia	Aramaiti	350
-27	85.7	V46 - Aino Planitia	Ohogetsu	175
-46.5	8105	V46 - Aino Planitia	Khotun	200

-48	88.3	V46 - Aino Planitia	Cailleach	125
-34	66.5	V46 - Aino Planitia	Unknown	105
-38.5	149.5	V47 - Artemis Chasma	Teteoinnan	125
-42	256	V52 - Helena Planitia	Unknown	105
-42.5	245.2	V52 - Helena Planitia	Nungui	150
-36	304.6	V54 - Nephys Mons	Persephone	120
-52.3	14.6	V56 - Lada Terra	Sarpanitum	170
-73	99	V57 - Fredegonde	Mykh-lmi	150
-58.5	163.5	V58 - Henie	Folta	150
-55.5	167	V58 - Henie	Utset	150
-53.5	291	V60 - Godiva	Obasi-Nsi	230
-51.5	289.5	V60 - Godiva	Tureshmat	150
-51	292	V60 - Godiva	Unknown	131.25

Table II. Data available for mapped circular lows.

#	Circular Low	Lat/Long	Mapped Area	Quad	Cycle 1	Cycle 2	Cycle 3	True Stereo	Synthetic Stereo
1	Zemlika	33.5S/50.0E	29.3S to 37.5S 54.0E to 46.0E	V45	yes	no	no	no	yes
2	Verdandi	5.5S/65.2E	1.0S to 10.0S 69.7E to 60.7E	V34	yes	yes	yes	yes	yes
3	Thouris	6.5S/12.9E	3.0S to 10.0S 8.4E to 17.4E	V32	yes	no	yes	yes	yes
4	Aramaiti	23.3S/82.0E	22.5S to 29.5S 88.5E to 79.5E	V46	yes	yes	yes	yes	yes
5	Ohogetsu	27.0S/82.0E	22.5S to 29.5S 88.5E to 79.5E	V46	yes	yes	yes	yes	yes

Table III. The circular lows mapped.

#	Circular Low	Lat/Long	Mapped Area	Quad	Diameter (km)	Central Depth (km)	Width of depression (km)	Annulus Width (km)	Raised Rims *
1	Zemlika	33.5S/50.0E	29.3S to 37.5S 54.0E to 46.0E	V45	150	0.5	120	50	yes
2	Verdandi	5.5S/65.2E	1.0S to 10.0S 69.7E to 60.7E	V34	180	1.0	155	20 - 50	yes
3	Thouris	6.5S/12.9E	3.0S to 10.0S 8.4E to 17.4E	V32	190	0.5 - 0.7	175	20 - 50	yes
4	Aramaiti	23.3S/82.0E	22.5S to 29.5S 88.5E to 79.5E	V46	350	0.1 - 0.2	267	25	yes
5	Ohogetsu	27.0S/82.0E	22.5S to 29.5S 88.5E to 79.5E	V46	190	0.1 - 0.2	115	15	yes

*Raised Rim: Parts of the circular low that are a higher elevation than the surrounding area.
The rim can be surrounding the whole circular low or just parts of it

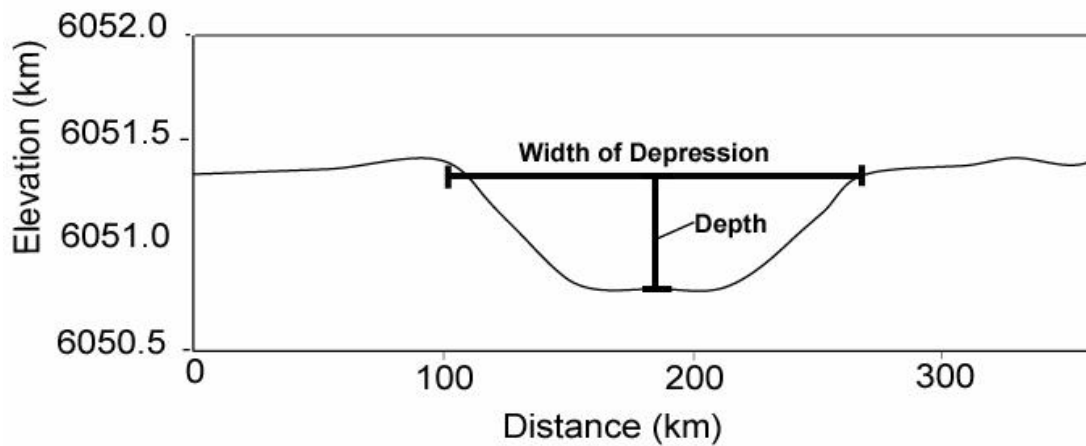
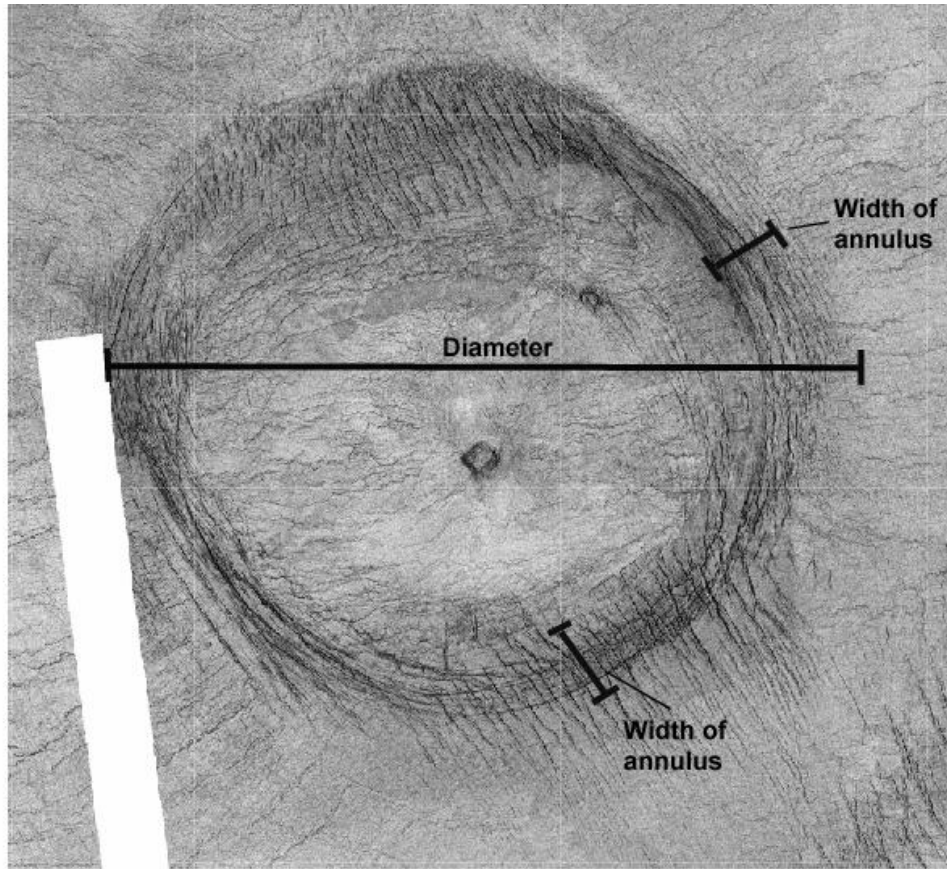


Figure 5. Left-illumination inverted SAR image of a circular low illustrating how I measured the diameter of the circular low and width of the annulus. Below the image is a topographic profile of the circular low illustrating how I measured the depth of the circular low's depression and the width of the depression.

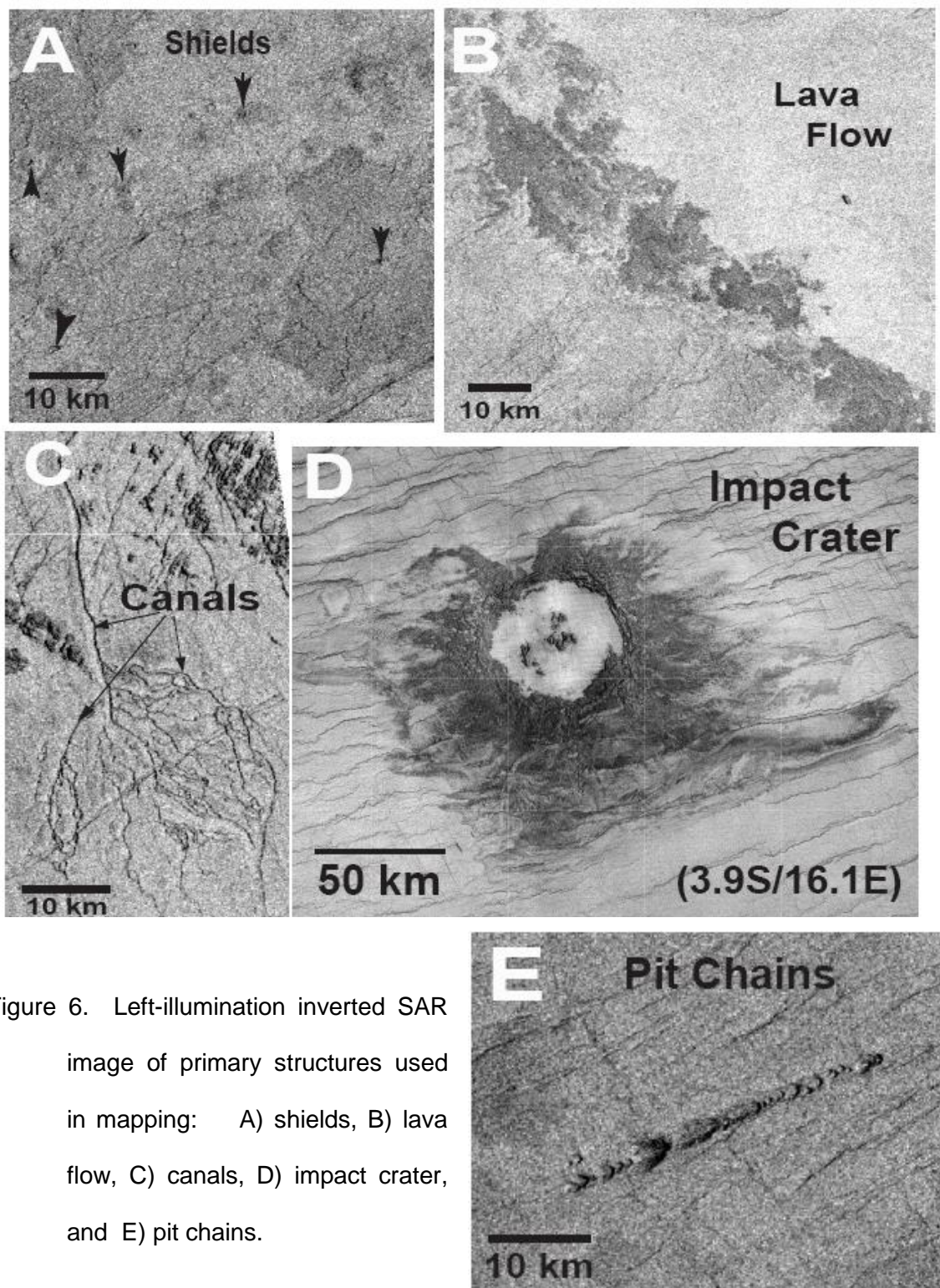


Figure 6. Left-illumination inverted SAR image of primary structures used in mapping: A) shields, B) lava flow, C) canals, D) impact crater, and E) pit chains.

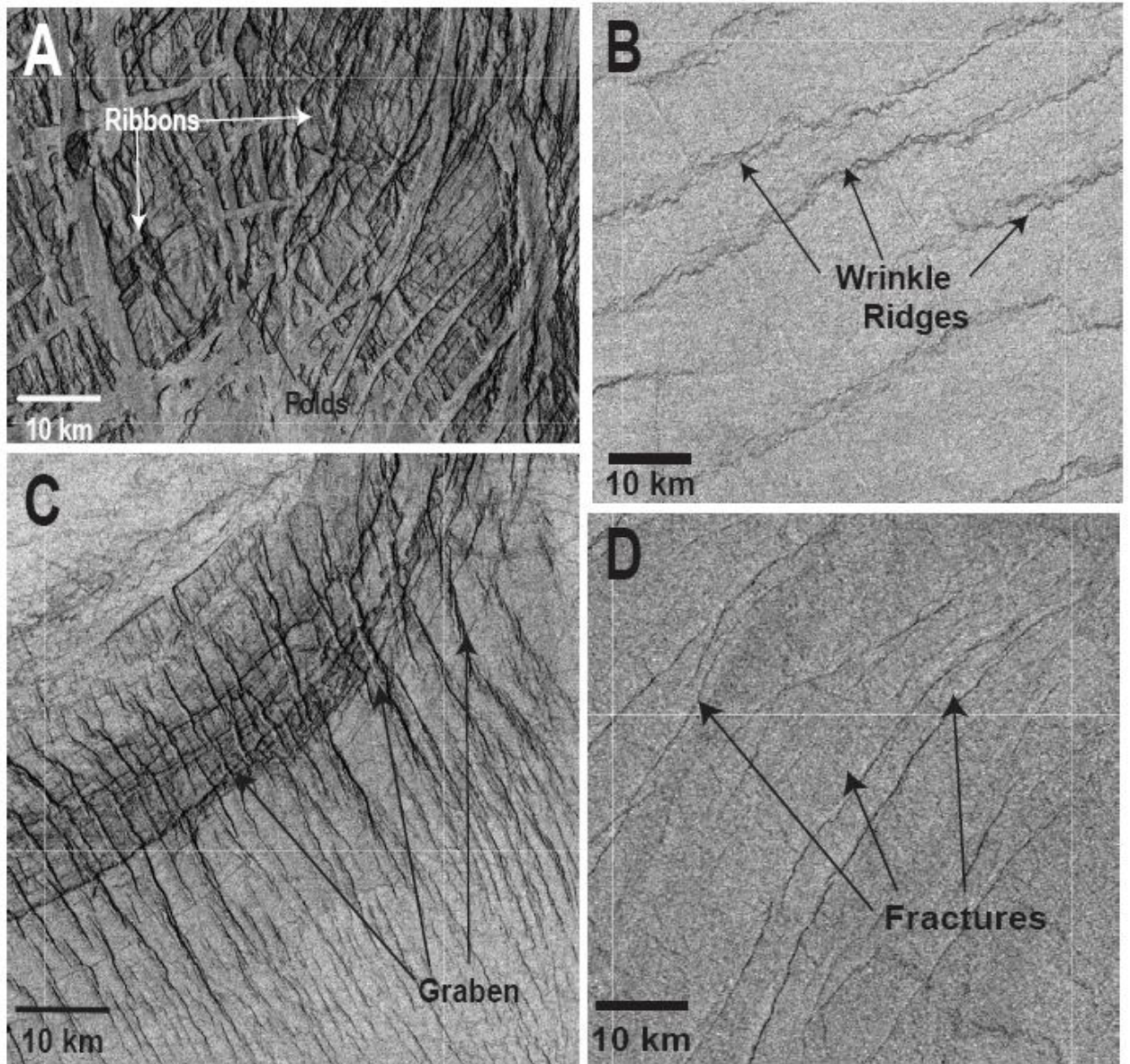


Figure 7. Left-illumination inverted SAR-images of secondary structures: A) ribbons and folds, B) wrinkle ridges, C) graben, and D) fractures.

Circular Lows

Five circular lows were mapped in detail, and each is discussed in turn here: Zemlika, Aramaiti, Ohogetsu, Verdandi, and Thouris. With the exception of Thouris, these circular lows are located in areas adjacent to tessera terrain. In each map area I mapped a region well outside of the selected circular low in order to place the circular lows in a regional spatial and temporal context.

Zemlika

Zemlika (33.5S/50.0E; 150 km diameter) occurs within the map area that extends from 29.3S to 37.5S and 54E to 46E (Figs. 8 and 9). The region represents a lowland that hosts large tessera ribbon-terrain inliers with west to northwest-trending folds and orthogonal ribbon fabric, and three pristine impact craters identified as Masako (30.2S/53.2E; 23.8 km diameter), Lockwood (32.9S/51.6E; 22.0 km diameter), and Purev (31.1S/46.4E; 11.6 km diameter). Zemlika lies within the tessera inliers. There is little to no disruption of the surrounding delicate tessera folds and ribbon fabrics; tessera fabric structural trends are collinear on either side of Zemlika. Regional fractures trend northeast and wrinkle ridges trend northwest. Shields and radar-smooth material occur variably across the map area.

Topographically Zemlika is marked by a 0.5 km-deep interior circular depression, 120 km wide, and a 0.5 km-high and 50 km-wide incomplete rim (Fig. 8). A well-defined concentric fracture suite defines Zemlika structurally. Concentric fractures occur along the rim walls as well as along the crest of the

rim. Along the northern margin of the circular low concentric fractures extend beyond the crest outside the rim. Concentric fracture spacing typically ranges from 1 to 2 km and from 150 to 270 degrees of the circular structure show spacing closer than 1 to 2 km. Nine lines of pit chains occur within the suite of concentric fractures from 150 to 270 degrees with lengths ranging from 20 to 80 km. From 0 to 60 degrees and from 270 to 360 degrees concentric fractures correlate spatially with the 0.5 km raised rim. Within the depression interior wrinkle ridges trend parallel to regional wrinkle ridges outside the circular low. Wrinkle ridges deform interior radar-smooth unit A, and units B, D, and undivided material outside the circular low.

The tracts of tessera terrain that lie 0.2 to 0.8 km above the base cover the northern part of the map area. The distinctive structural fabrics, folds, and orthogonal ribbons characterize the tessera terrain (Hansen and Willis, 1996, 1998). Folds trend west-northwest, with lengths 10 to 145 km and wavelengths of 5 to 20 km; ribbons with wavelengths of 1 to 4 km trend orthogonal to folds. An intratessera region forms the radar smooth area parallel to the fold troughs.

Fractures occur in the southwest region of the map area, the northwest region just northwest of Zemlika, and the northeast region north of Masaka (30.2S/53.2E). The southwest region has fractures with lengths ranging from 10 to 250 km and spacing of 1 to 30 km. These fractures also include locally concentric fractures with 1 to 5 km spacing. Fractures in the northwest and northeast region trend east-northeast and are spaced 1 to 10 km with lengths ranging from 10 to 60 km. The northwest region also contains fractures that

trend northwest with spacing of 5 km and lengths ranging from 10 to 25 km. The fractures cut the undivided material and material unit D. Suites of wrinkle ridges occur in the northeast and northwest, and to the south around Zemlika. Wrinkle ridges south of impact crater Masaka are surrounded by tessera terrain and deform into the units D and undivided. Wrinkle ridges trend northwest with lengths of 1 to 50 km and spacing of 1 to 10 km. These wrinkle ridges have the same orientation as the wrinkle ridges in the interior of Zemlika. These wrinkle ridges deform units B and D.

The geologic map clearly shows that Zemlika formed after the tessera-terrain. Zemlika cuts the delicate tessera structural fabric in cookie-cutter manner with little to no disruption to the surrounding tessera terrain folds or ribbons; within the region of Zemlika, tessera fabrics are absent, presumably obliterated. Interior wrinkle ridges parallel the regional suite of wrinkle ridges, indicating that the interior of Zemlika is flooded with a thin layer of material, here called unit A. Wrinkle ridges formed after Zemlika and after minor interior flooding. The nine lines of pit chains post-date formation of the circular low, or formed later during circular low formation because the pit chains occur in the suite of concentric fractures that make up Zemlika. The fractures and wrinkle ridges also postdated the canals as illustrated by crosscutting relations.

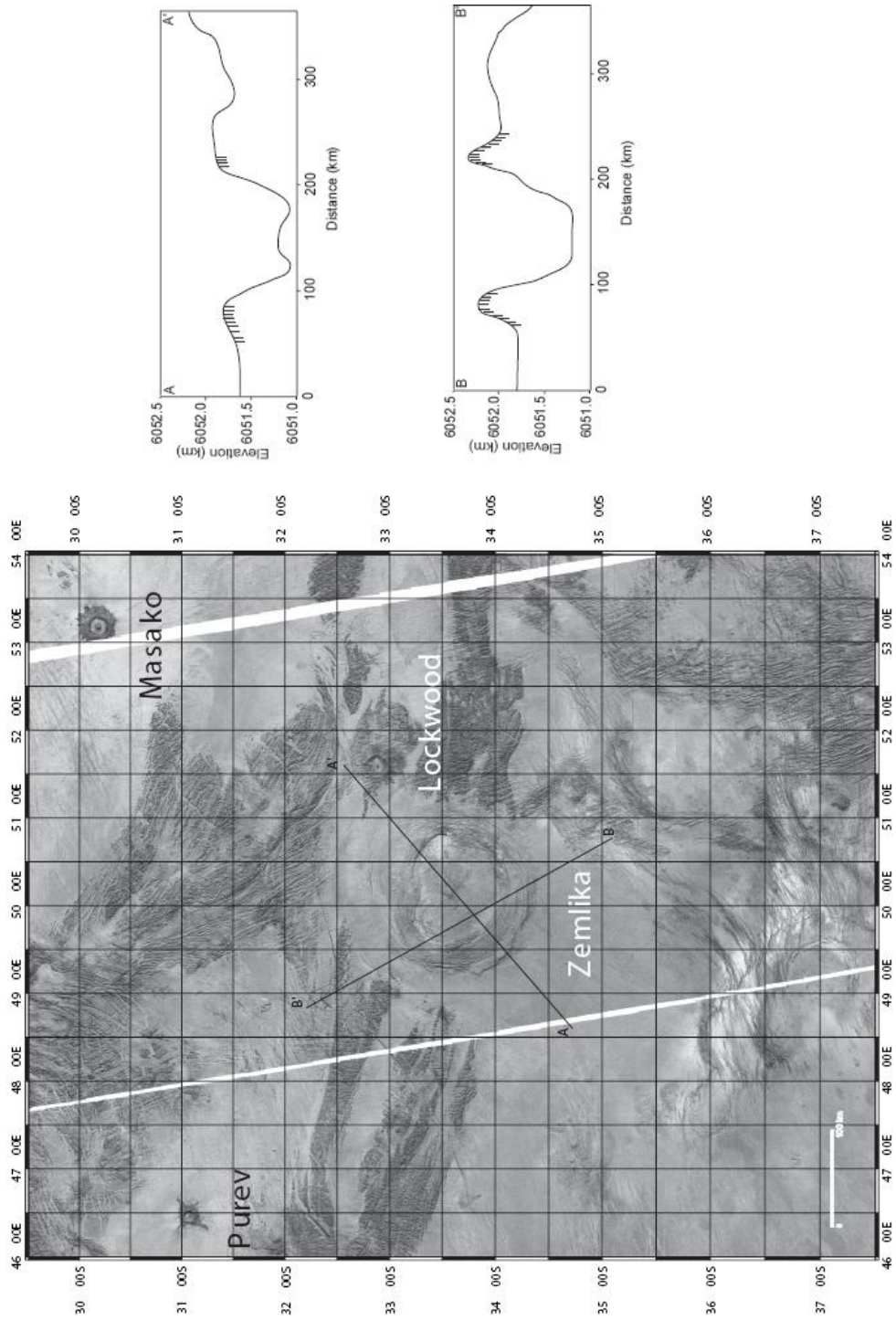


Figure 8. Left-illumination inverted SAR image of Zemlika (33.5S/50.0E; 150 km diameter) with topographic profiles.

Topographic profiles have pattern added to them to indicate zone of annular fractures.

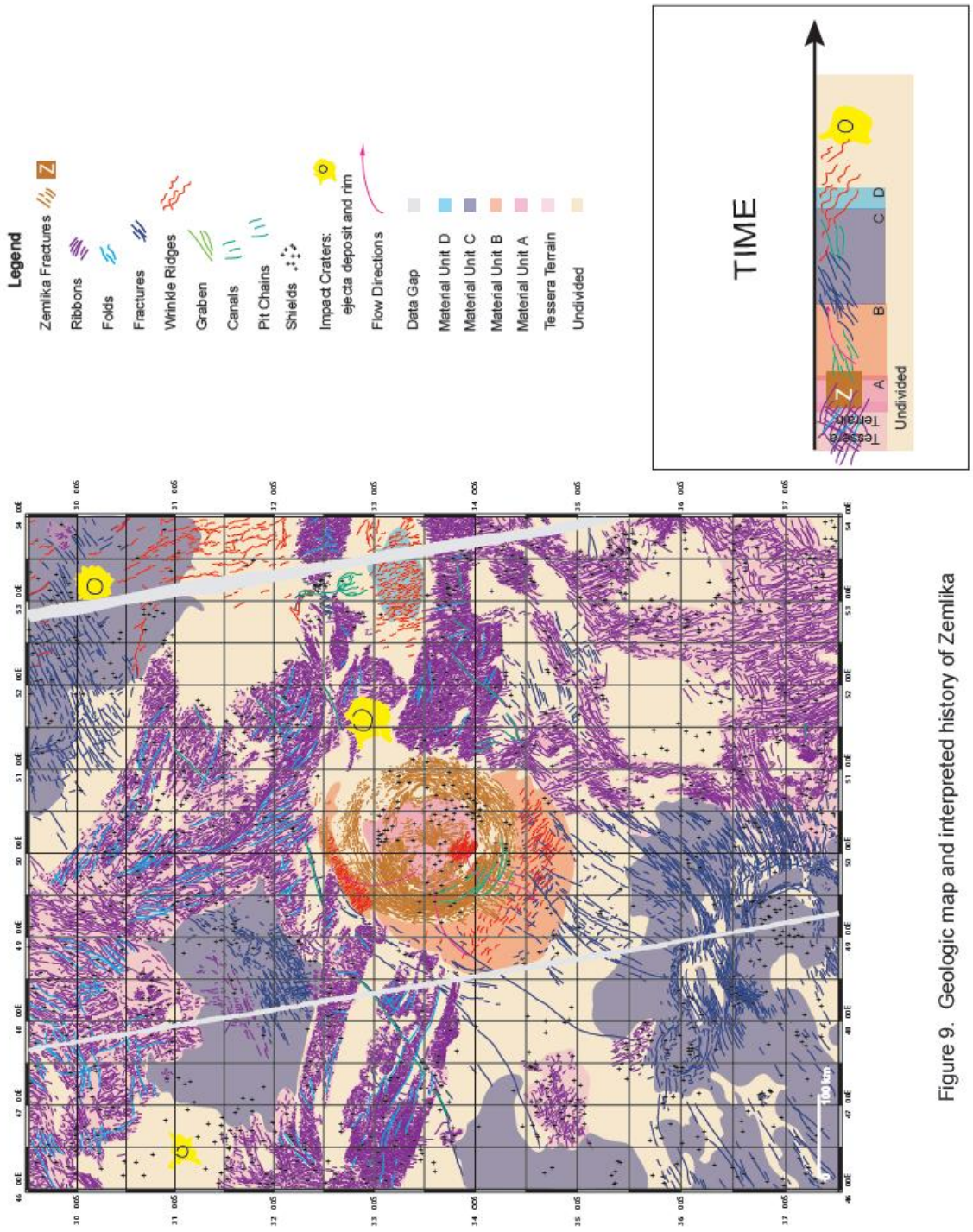


Figure 9. Geologic map and interpreted history of Zemlika

Verdandi

Verdandi (5.5S/65.2E; 180 km diameter) occurs within the map area that extends from 1.0S to 10.0S and 70.0E to 46.0E (Figs. 10 and 11). The region hosts ribbon-terrain tessera inliers with east-northeast-trending folds and orthogonal ribbon fabrics, and two pristine impact craters, Juliot-Curie (1.7S/62.4E; 100.9 km diameter) and Andreianova (3.0S/69.0E; 69.5 km diameter). Tessera inliers surround Verdandi. Regional fractures trend west-northwest and east-northeast; and shields occur variably across the map area.

Topographically, Verdandi is marked by a 1 km deep interior depression, 155 km wide, and a 0.2 to 0.4 km high and 20 to 50 km wide rim (Fig. 10). A well-defined concentric fracture suite defines Verdandi structurally. The concentric fractures occur along the interior rim walls as well as along the crest of the northeast rim. Concentric fracture spacing typically ranges from 1 to 10 km and shows wider spacing from 0 to 90 degrees and from 270 to 360 degrees. Linear fractures trending west-northwest from 210 to 300 degrees surrounding the concentric fractures. Linear northeast trending fractures cut the southwest part of the circular low. The central interior region contains east-trending fractures and north trending wrinkle ridges.

Tessera terrain lies 0.4 to 1 km above the surrounding area and dominantly covers the map. Tessera folds trend east-northeast, orthogonal to ribbon trends. Intratessera material is the radar smooth region parallel to the fold troughs (fold length: 10 to 190 km). The northeast corner of the map has ribbon wavelengths that are 40 km apart due to flooding; whereas the rest of the tessera

has wavelength of 1 to 10 km. Deformed by fractures unit material A occurs near the edges of the tessera terrain east of Verdandi. A suite of fractures northwest and southeast of Verdandi parallel the ribbon terrain fabric trending west-northwest. The southeast corner of the map area displays a suite of dominantly east-trending fractures with some concentric fractures that cut the undivided material and unit B.

The geologic map provides clear evidence that Verdandi post-dates the tessera terrain formation. The fractures in the interior of the structure appear to post-date Verdandi because these fractures trend parallel to fractures that cut the southeast concentric fractures of Verdandi and the fractures east of Verdandi. The suite of fractures in the southeast corner of the map area post-dated tessera terrain formation. There is not enough information to determine whether or not the suite of fractures in the southeast corner formed before or after Verdandi, but their formation does not appear to relate directly to the formation of Verdandi. This fracture suite might post-date Verdandi formation, because these fractures dominantly trend in the same orientation as the other regional fractures.

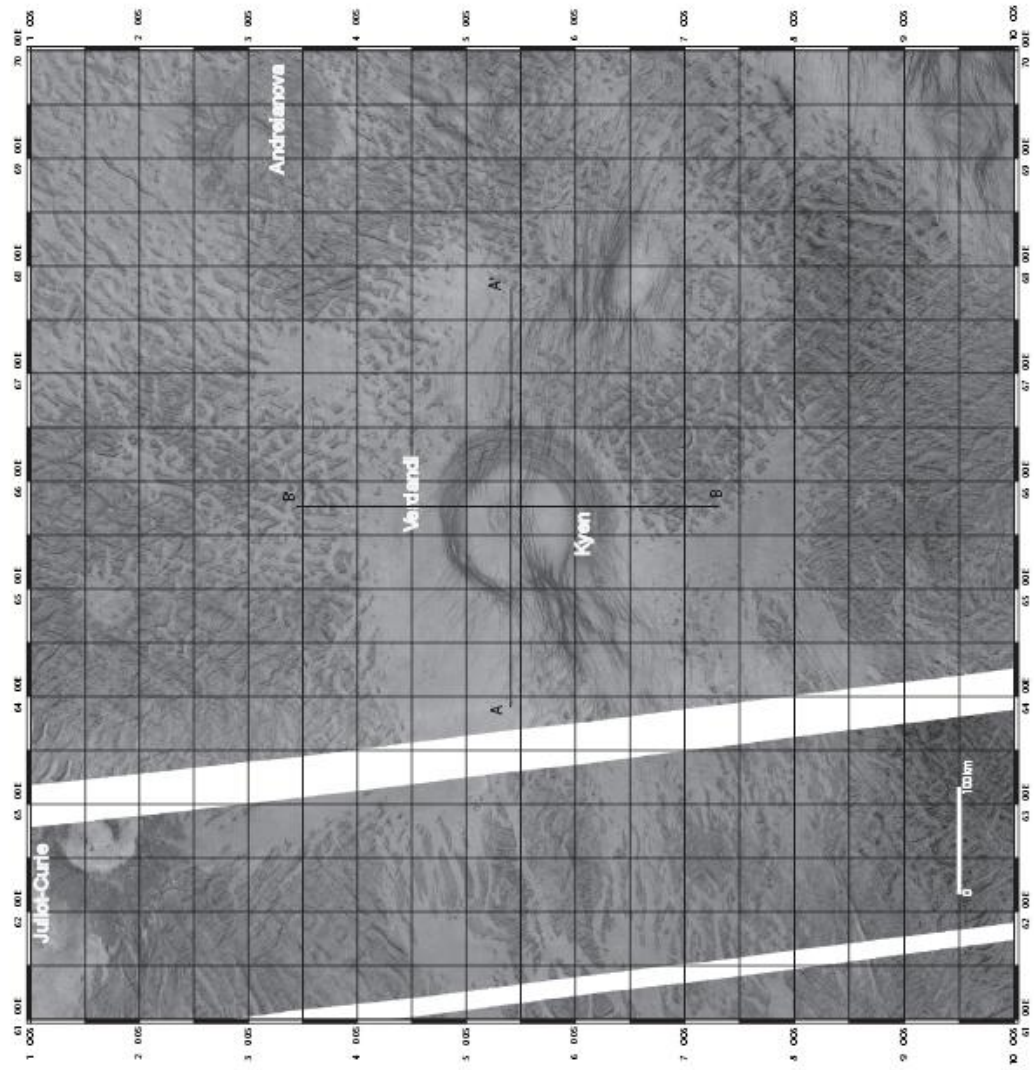


Figure 10. Left-illumination inverted SAR image of Verdandi (33.5S/50.0E; 150 km diameter) with topographic profiles.

Topographic profiles have pattern added to them to indicate zone of annular fractures.

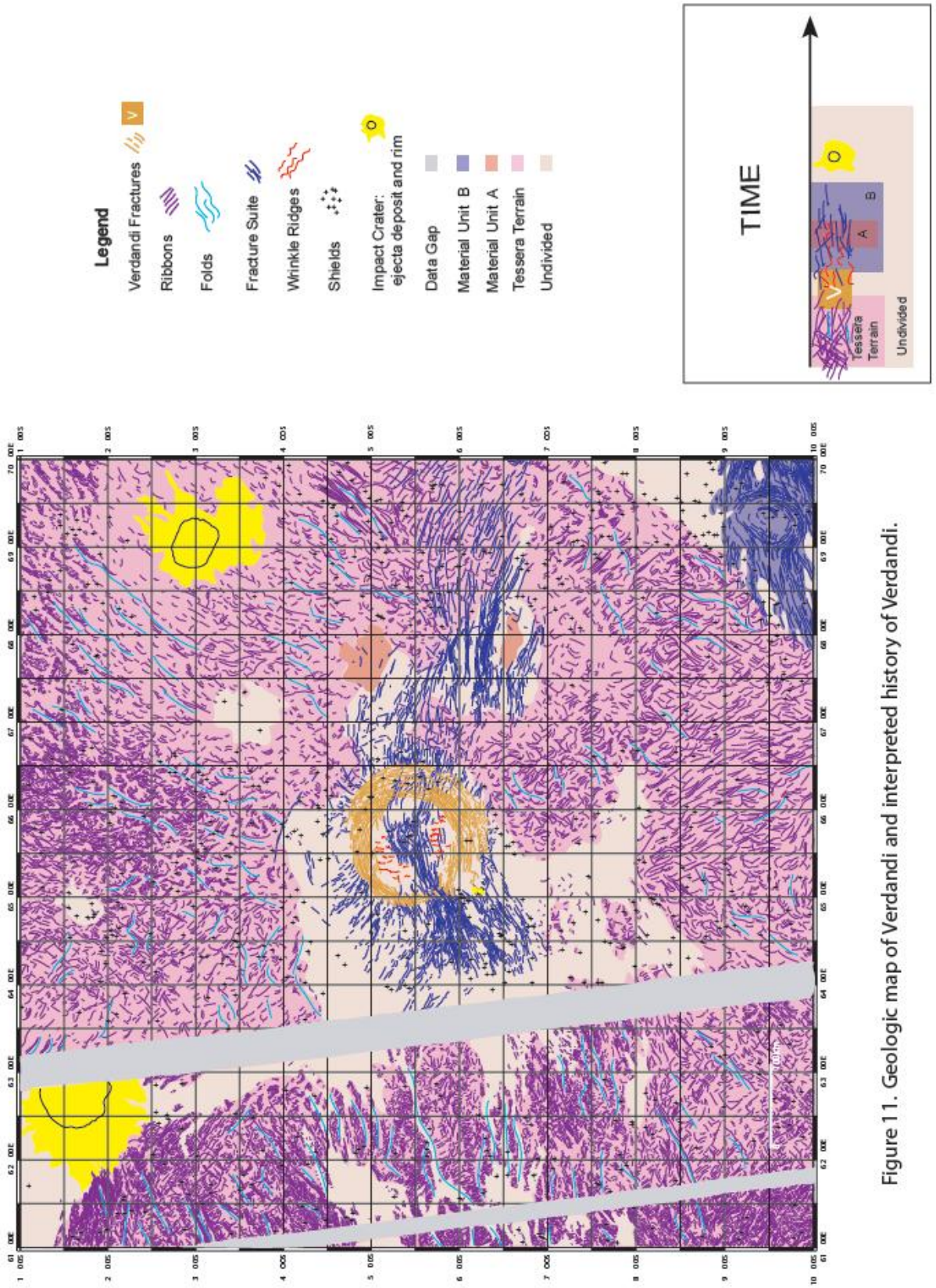


Figure 11. Geologic map of Verdandi and interpreted history of Verdandi.

Thouris

Thouris (6.5S/12.9E; 190 km diameter) occurs within the map area that extends from 3S to 10S and 8.4E to 17.4E (Figs. 12 and 13). This map area also hosts two moderately large coronae, Atargatis (8.0S/8.6E; 350 km diameter) and Kuan Yin (4.3S/10.0E; 310 km diameter), and one impact crater, Carreno (3.9S/16.1E; 57.0 km diameter). Well-developed regional wrinkle ridges trend east-northeast orthogonal to north-northwest trending regional fractures, which concentrate in the southeast corner of the map area. A 50 km-wide zone of north-striking regional fractures transects the middle of Thouris. Within the fracture zone, 10 to 30 km-long and 1 to 2 km-wide graben cut the north and south rim of Thouris, and parallels the regional fracture suite.

Topographically Thouris is defined by a 0.5 to 0.7-km deep, 175 km-wide depression surrounded by a 0.1 to 0.2 km-high and 10 to 20 km-wide rim that surrounds most of the structure (Fig. 12). Concentric fractures, which structurally define Thouris, occur along the inside wall and rim crest. Along the north and south margins of Thouris, graben (1 to 2 km width, 5 to 20 km length) trend northwest cutting the rim and interior wall of the depression. The central region of Thouris hosts two small volcanoes with minor associated flooding material unit D. Interior wrinkle ridges trend parallel to regional wrinkle ridges, indicating that wrinkle ridge formation post-dated Thouris formation.

The regional structures on the map area are the coronae, wrinkle ridges, fractures, and impact crater. Atargatis Corona rises about 0.7 km above the base and cuts into unit material A, where as Kuan Yin Corona rises 0.1 km above

its surroundings; a small area on the corona rises 0.2 km above the base and cuts into material unit B. Wrinkle ridges occur across the map area from 0.7 km below the base to 0.7 above the base. A southeast-trending suite of fractures has an elevation of 0.7 km above the base and cuts material unit E and the undivided material unit. The central elevated region of Atargatis is surrounded by concentric fractures with spacing of 1 to 10 km. North-northwest-trending fractures with lengths of 5 to 70 km and spacing of 1 to 5 km cut the central region of Atargatis. Atargatis cuts into material unit A and its concentric fractures cut into material unit C. Graben cut the northern part of Atargatis with lengths of 5 to 70 km and spacing of 5 to 10 km. Kuan Yin Corona, in the northwest corner of the map, hosts north-northwest-trending fractures spacing from 1 to 10 km. Concentric fractures surround the central region of Kuan Yin with spacing of 1 to 10 km. North-northwest-trending graben cut the concentric fractures and the interior of the structures with lengths of 1 to 35 km and spacing of 1 to 10 km. Elevated areas, such as the central regions of the two coronae and the southeast suite of fractures show fewer wrinkle ridges than the surrounding, lower, areas. A suite of fractures that occurs in the southeast corner of the map trends north-northwest with lengths 10 to 70 km and spacing of 1 to 10 km. Fractures east of Thouris appear to trend north-northwest with similar lengths and spacing as the southeast suite of fractures. These fractures appear to cut a suite of fractures north of Thouris, which trend dominantly north with lengths of 5 to 35 km and spacing of 1 to 10 km. Impact crater Carreno occurs in the northwest corner of

the map area and surrounding by material unit F, which might be interpreted as a halo deposit.

Thouris likely post-dates the formation of the two large coronae in the western portion of the map area because Thouris trends do not appear diverted by coronae trends, although the spatial separation of the three features makes robust relative timing relations difficult to constrain. It is possible for Thouris to predate or form at the same time as the coronae because the coronae and Thouris do not cut into each other, they touch. If Thouris formed before or at the same time as Kuan Yin and Atargatis, then Thouris' circular shape might be deformed due to the effects caused from Kuan Yin and Atargatis' formation. The graben post-dates the formation of Thouris because they cut Thouris' concentric fractures. The graben that cut the two coronae may have formed at the same time as the graben that cut Thouris because the coronae graben trend north-northwest, the parallel to Thouris' graben. The graben may also have formed at the same time as the suite of fractures in the southeast region given their parallel trend. The suite of fractures north of Thouris predates the formation of Thouris because Thouris cuts into these fractures. The fractures appear to have formed at the same time as Kuan Yin's formation because these fractures are following the orientation of the concentric fractures. The suite of fractures in the southeast corner of the map area (north-northwest trending) likely post-dated the formation of Thouris because these fractures trend in the same orientation as the fractures that cut Thouris' concentric fractures. The wrinkle ridges likely post-date and occur within the interior of Thouris the formation of the north-northwest trending

suite of the fractures because the wrinkle ridges deform flows that post-date the coronae, Thouris, and the regional fractures. The wrinkle ridges all trend dominantly in the same orientation across the map area indicating they likely formed at the same time. The impact crater Carreno post-dated the formation of the wrinkle ridges because ejecta deposits locally pond against and cover the wrinkle ridges.

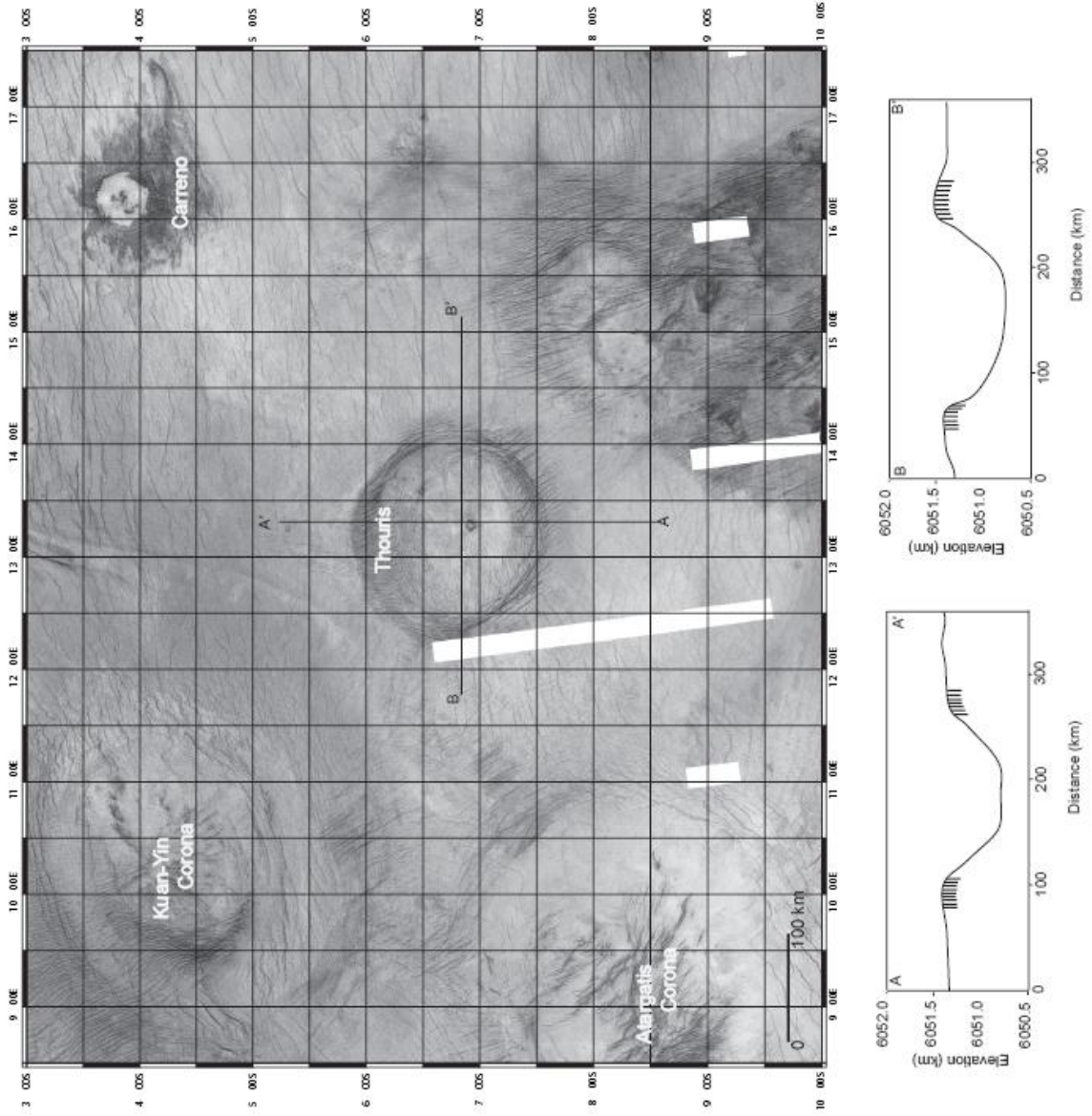


Figure 12. Left-illumination inverted SAR image of Thouris (6.55/12/9E; 190 km diameter) with topographic profiles.

Topographic profiles have pattern added to them to indicate zone of annular fractures.

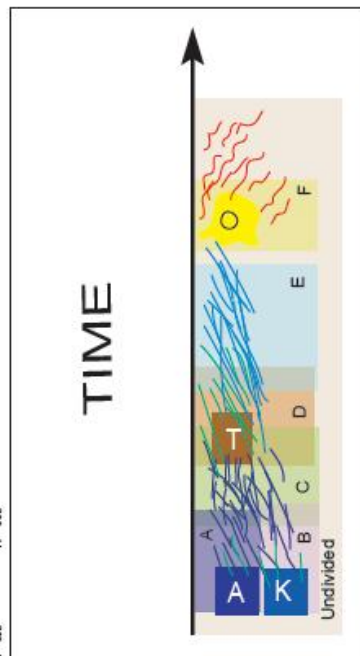
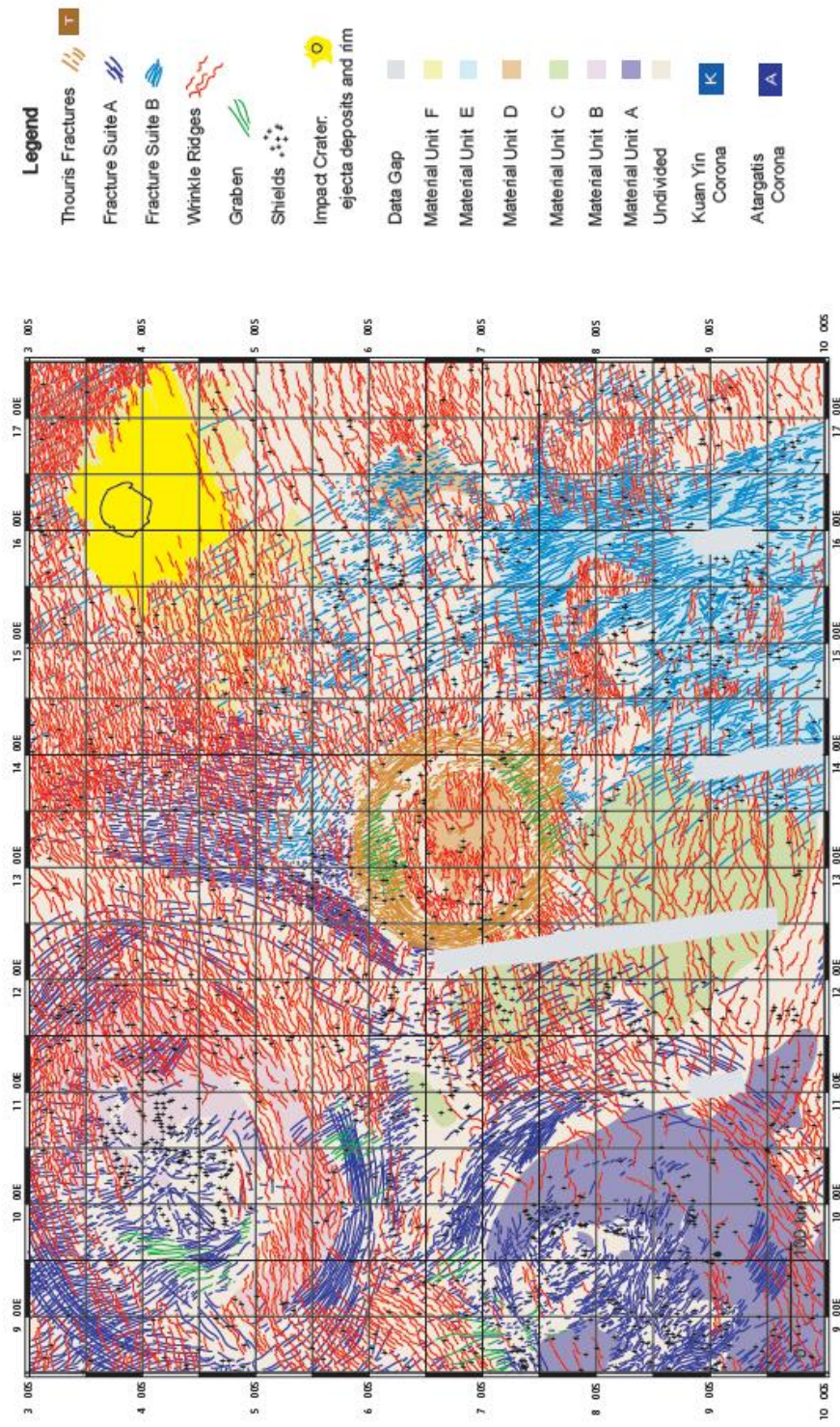


Figure 13. Geologic map of Thouris and interpreted history of Thouris.

Aramaiti and Ohogetsu

The Aramaiti map area, which extends from 22.5S to 29.5S and 88.5E to 79.5E, hosts two circular lows, *Aramaiti* (23.3S/82.0E; 350 km diameter) and *Ohogetsu* (27.0S/85.7E; 175 km diameter), as well as ribbon-tessera terrain, and one impact crater, Emilia (26.5S/88.2E; 12.5 km diameter) (Figs. 14 and 15). Regional fractures trend east-northeast, and regional wrinkle ridges trend east-northeast and northwest, defining two suites. Wrinkle ridges are best developed in the northeast corner of the map area. Wrinkle ridges also cut the radar smooth undivided material unit that surrounds Ohogetsu and a radar smooth unit material in the northwest corner of the map touching the edge of Aramaiti's rim (Unit E) and the interior of Aramaiti (Unit C).

Topographically Aramaiti is defined by a 0.1 to 0.2 km-deep and 267 km-wide depression, and a 0.4 km-high and 25 km-wide rim (Fig. 14). A 100 km-wide (0.5 km high) dome is surrounded by an 80 km-wide and 0.1 to 0.2 km-deep moat which lies within the interior. The dome surface preserves subdued radial fractures. Aramaiti cuts tessera terrain along its northeastern margin; delicate tessera-terrain structural fabrics are obliterated within Aramaiti, but appear pristine northeast of Aramaiti. A well-developed suite of concentric fractures structurally defines Aramaiti. From 240 to 330 degrees concentric fractures spaced 1 to 6 km occur along the inside rim wall. From 30 to 210 degrees concentric fractures spaced 1 to 2 km occur along the inside rim wall. The concentric fractures cut material unit A, and the north part of Aramaiti has blocky radar-rough material mapped as material unit B.

Ohogetsu is defined by a 0.1 to 0.2 km-deep, 115 km-wide depression with a small central peak, 0.4 km-high and 15 km-wide at the rim; the rim is partially developed around the structure and cuts into tessera terrain (Fig. 14). Interior wrinkle ridges that surround the central peak trend parallel to regional wrinkle ridges. Well-defined concentric fractures define Ohogetsu structurally. Concentric fractures are most tightly spaced (1 to 2 km) and best developed from 0 to 90 degrees and from 300 to 360 degrees, and occur along the topographic rim wall and crest, extending locally outside the rim. From 0 to 90 degrees and from 300 to 360 degrees concentric fractures occur along the basin floor.

The regional structures are tessera terrain, wrinkle ridges, fractures, and the impact crater. Topographically, tessera terrain lies 0.2 to 0.7 km above the surrounding area. Tessera terrain occurs diagonally (northwest) across the central region of the map area with distinctive structural fabrics comprised of ribbons and folds (Hansen and Willis, 1996; Hansen and Willis, 1998). The ribbons trend northwest and northeast with lengths of 8 to 67 km and wavelengths of 5 to 15 km. The folds trend northwest and northeast with lengths of 15 to 40 km and wavelengths of 1 to 25 km. There are two suites of wrinkle ridges with different orientation and spacing. The west side of the map contains wrinkle ridges that trend dominantly northwest with lengths of 10 to 75 km and spacing of 5 to 15 km. A suite of wrinkle ridges on the east side of the map displays tighter spacing. The wrinkle ridges trend dominantly east-northeast with lengths of 10 to 100 km and spacing of 1 to 15 km. Fractures occur west and south of Aramaiti and trend dominantly east-northeast. Fractures extend 10 to

180 km with spacing of 5 to 15 km. There are also some fractures southeast of Aramaiti that trend northwest and cut Aramaiti. The fractures have lengths 110 to 250 km with spacing of 10 to 70 km. The impact crater Emilia occurs west of Ohogetsu.

Aramaiti and Ohogetsu both formed after the local tessera terrain; both features cut tessera fabric and obliterate fabric within their rims and interiors, yet delicate fabric trends within the tessera-terrain lack disruption immediately away from each circular low. The northwest trending fractures post-date the formation of the Aramaiti and Ohogetsu because they cut Aramaiti and Ohogetsu's concentric fractures. The radar-smooth material, material unit E, post-dates the regional fractures because the material appears to be covering some of the regional fractures that cut the circular low structures. Both suites of wrinkle ridges most likely formed at the same time. Both suites of wrinkle ridges also post-dated the circular lows and the regional fractures because they deform material that locally covers the fractures. The impact crater post-dates the wrinkle ridges because the crater ejecta appears to pond against local wrinkle ridges.

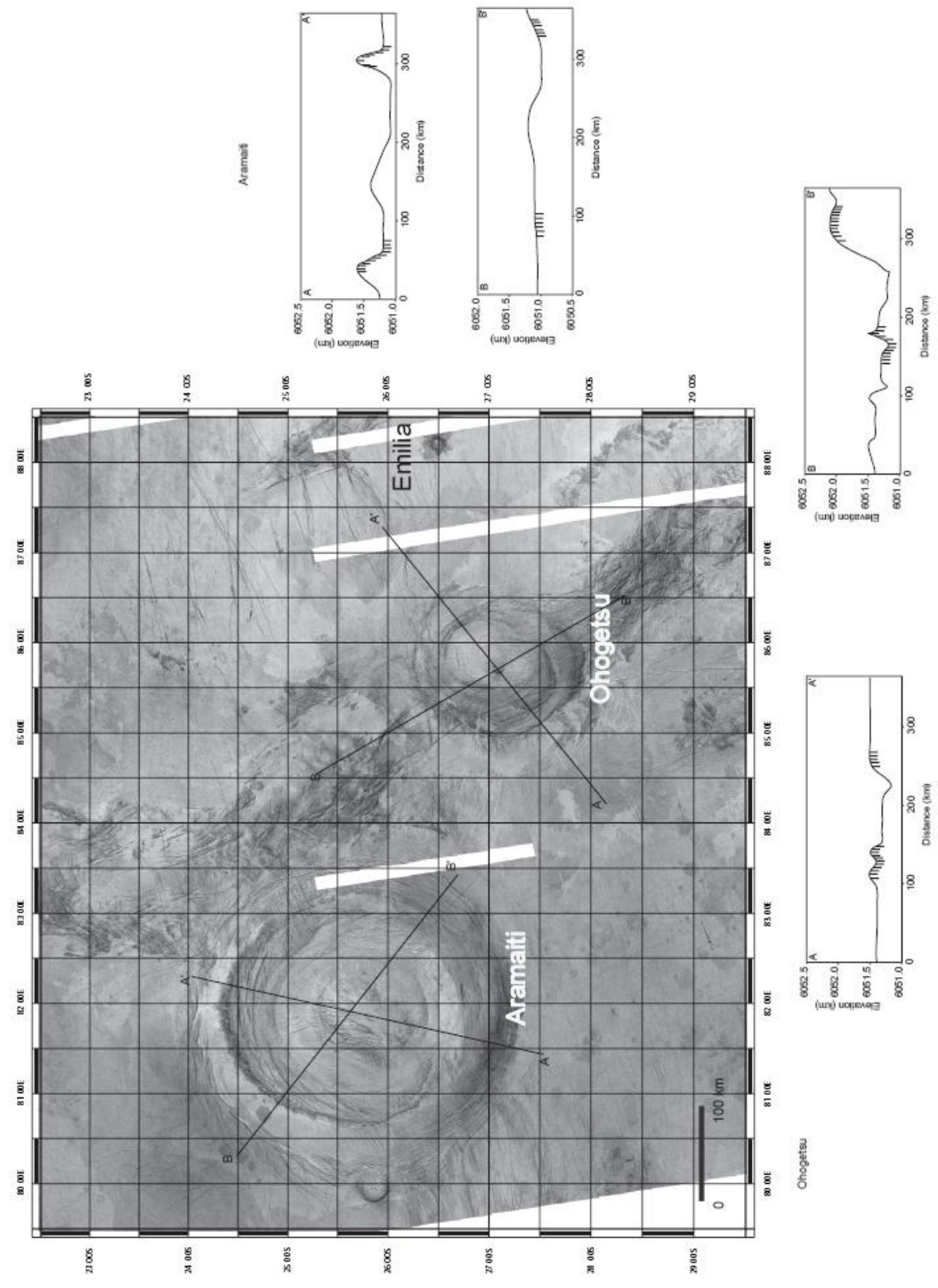


Figure 14. Left-illumination inverted SAR image of Aramaiti (23.35/82.0E; 350 km diameter) and Chogetsu (27.05/82.0E; 190 km diameter) with topographic profiles. Topographic profiles have pattern added to them to indicate zone of annular fractures.

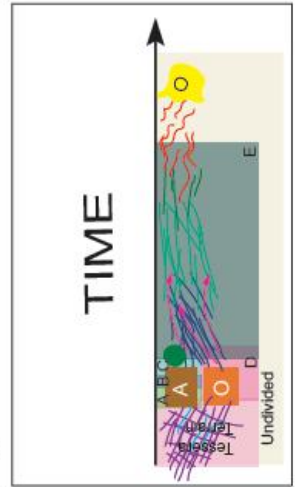
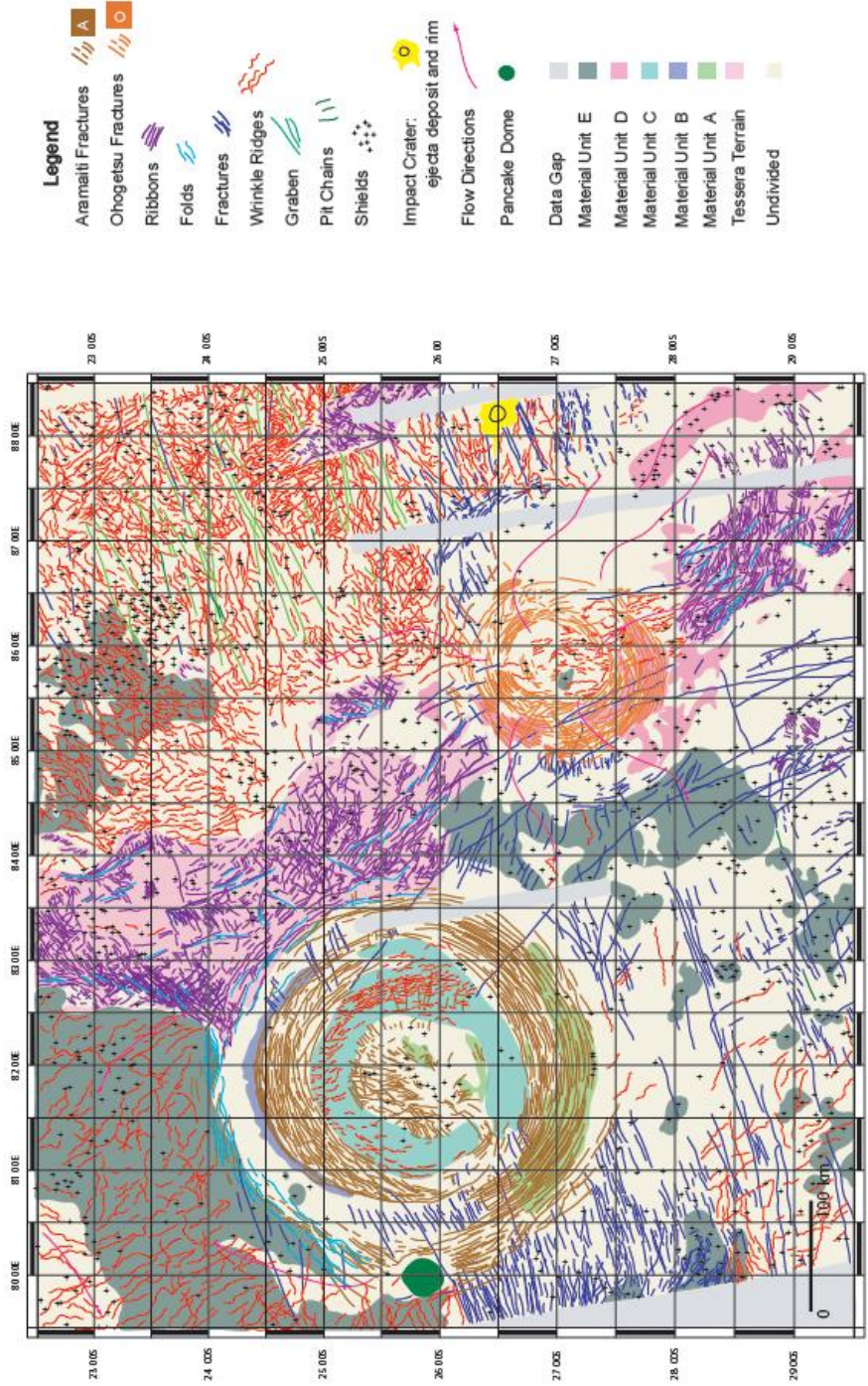


Figure 15. Geologic map and interpreted history of Aramaiti and Ohogetsu

Common Characteristics

The five circular lows mapped herein share the following characteristics: 1) a shallow amphitheater-like depression (less than or equal to 1 km), 2) concentric fractures, 3) lack of radial fractures, and 4) lack of disturbance outward to surrounding areas (Fig 16). All five circular lows formed relatively early in the locally recorded history. Four of the circular lows cut tessera terrain, whereas the fifth may cut concentric fractures of two coronae. Thouris and Ohogetsu both lack fractures in their central region, whereas the other three have fractures cutting their central region. All of the circular lows, with the exception of Verdandi, display minor flooding in their interior or their immediate surroundings.

Stofan and Guest (2003) constructed a 1:5 million scale geologic map of the Aino Planitia Quadrangle (V-46), which hosts Aramaiti and Ohogetsu. Their map displays only part of Aramaiti; the rest of Aramaiti is in the Ix Chel Chasma Quadrangle (V-34). My map covers parts of V-46 and parts of V-34 in order to display all of Aramaiti with Ohogetsu. Stofan and Guest's map (2003) focuses more on the material units surrounding the circular lows rather than the tectonic structures. The map does not display the fractures occurring at Aramaiti and Ohogetsu in as much detail like my map does, however Stofan and Guest do indicate there are fractures occurring at Aramaiti and Ohogetsu. The material units for Aramaiti and Ohogetsu on Stofan and Guest's map (2003) are similar to where I marked my material units. Stofan and Guest's map (2003) has the material units characterized in more detail than my map. Overall, both maps display common structures and units concerning the circular lows. The main

differences between the maps are the amount of detail shown regarding the tectonic structures and material units.

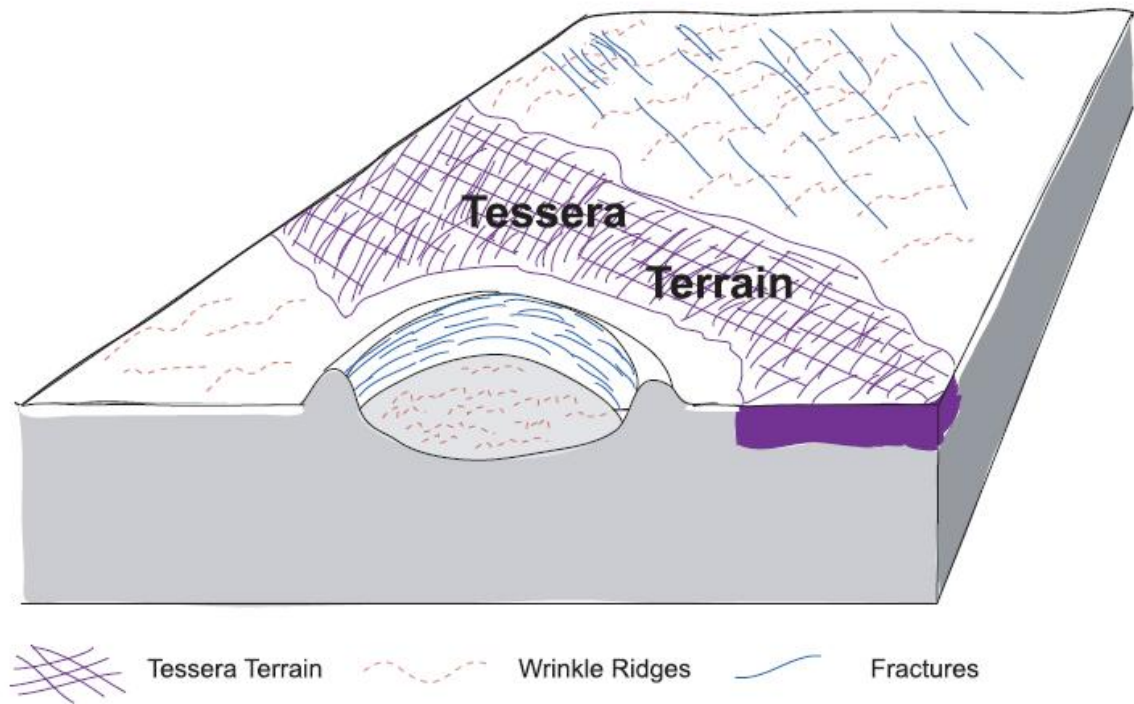


Figure 16. A cartoon block diagram illustrating characteristic features of circular lows.

The block contain 1) concentric and linear fractures, 2) tessera terrain, 3) wrinkle ridges and 4) flood lavas in the interior of circular low. The circular lows has concentric fracture, cookie-cutting truncation of tessera terrain, lack of radial fractures, shallow amphitheater-like depression (less than or equal to 1 km), lack of disturbance to immediately surrounding the circular low, and a rim.

Analysis

The wide range of coronae characteristics gives way to different interpretations about how coronae form. The most common hypotheses are: diapirs, calderas, and impact craters (Schaber and Boyce, 1977; Campbell et al., 1979; Campbell and Burns, 1980; Jurgens et al., 1980; Marsursky et al., 1980; Grieve and Head, 1981; Head and Solomon, 1981; Barsukov et al., 1986; Nikolayeva et al., 1986; Basilevsky, 1987; Janes et al., 1992; Stofan et al., 1992; Squyres et al., 1992; Koch, 1994; Cyr and Melosh, 1993; Koch and Manga, 1996; Stofan et al., 1997; DeLaughter and Jurdy, 1999; Hansen, 2003, Vita-Finzi, 2004; Hamilton, 2004). The information gathered from mapping the five circular lows enables me to interpret which hypothesis best explains their formation.

Diapir Hypothesis:

Scientists commonly interpret that coronae formed from an endogenic process related to upward movement of mantle diapirs that cause surface deformation (Janes et al., 1992; Stofan et al., 1992; Squyres et al., 1992; Koch, 1994; Cyr and Melosh, 1993; Koch and Manga, 1996; Stofan et al., 1997; DeLaughter and Jurdy, 1999; Hansen, 2003). Diapirs form in the mantle due to density contrasts caused by difference in temperature, composition, degree of partial melt, or other factors. Previous workers used experimental techniques, analytical models and finite-element models to study the formation of diapiric structures (Withjack and Scheiner, 1982; Cyr and Melosh, 1993; Koch and Manga, 1996) (Fig. 17). To determine whether or not circular lows could have

formed from diapirs, three diapiric models were studied: Withjack and Scheiner (1982), Cyr and Melosh (1993), and Koch and Manga (1996). Studying these three models, and comparing their results to the geologic histories of the circular lows that emerged from geologic mapping, allows me to evaluate a diapiric hypothesis for each circular low.

Withjack and Scheiner (1982) investigated the behavior of regional strain on domical fault patterns using experimental and mathematical models. The experimental scale model involved circular doming under different conditions of local and regional stress fields. Faults occurred in all the experiments, and were classified by 1) general appearance (jagged, straight, sinuous-short), 2) displacement, and 3) fault orientation relative to local direction of greatest shortening. The mathematical model of circular doming used four geologic conditions: 1) the original layer of rock overlying the diapir was a thick plate; 2) the plate consisted of homogeneous, isotropic, and linearly elastic material; 3) the plate's edge was clamped from the side and had uniform pressure applied along its base to simulate doming; 4) Anderson's (1942) relationship was used to predict the fault patterns produced by doming (Fig. 18). The mathematical and experimental results of domes formed in the presence of regional stress were similar. The domes displayed the structure having radial fractures (normal faults) formed in the central region surrounded by concentric fractures (thrust faults) creating a circular shape. With imposed regional stress fields added, parallel fractures (normal faults) formed in the central region surrounded by concentric fractures (thrust faults), creating either a half circle or no concentric fractures.

The results from the experimental and mathematical models were similar, indicating that a diapir can create radial fractures on the crest of the dome and be surrounded by concentric fractures. Adding local stresses will change the features of the structure, lacking radial fractures, and will likely change its overall circular shape. The authors do not interpret the behavior the dome over time. However, implicit in their results the relationship that radial fractures are generally older than concentric fractures defines the dome margin.

Cyr and Melosh (1993) analyzed the behavior of stress on tectonic features, such as normal and thrust faults, in Oduduwa Corona (11.0S/211.5E; diameter: 150 km), Beyla Corona (26.0N/16.0E; diameter: 400 km), and an unnamed corona (9.5S/69.0E; diameter: 85 km), and compared these features to Mars' Alba Patera (40.8N/109.6W). To evaluate the diaper hypothesis, the authors examined the behavior between regional and local corona-induced stresses and lithospheric thickness to determine if they could produce fracture systems similar to those of the specified coroneae on Venus. Cyr and Melosh were able to recreate these fault patterns by a two-stage model: upwarp for young coroneae and surface loading for mature coroneae. Upwarping was caused by a diapir pushing the lithosphere upward and surface loading was caused by the accumulation of volcanic material (Fig. 19). Their model employed the following assumptions: 1) all layers were isotropic and homogeneous; 2) the coroneae evolutionary sequence is based on the sequence proposed by Squyres et al., 1992 (Fig. 17); and 3) the material beneath the lithosphere had a density equal to the lithosphere itself, enabling the surface loads' stress orientation and

magnitudes to become time-independent. To test their model, Cyr and Melosh used a lithospheric thickness of 10 km and coronae with a diameter 200 km. The authors evaluated four models: 1) upwarp; 2) upwarp with added regional stress; 3) surface loading; and 4) surface loading with added regional stress. The upwarp stage illustrated radial normal faults to the corona's central region surrounded by an annulus of thrust faults. The upwarp with added regional stress made the radial normal faults become parallel and the annulus of thrust faults evolved from a full circle annulus to a half circle or even no annulus depending on the amount of added regional stress. The surface loading model resulted in the formation of central thrust faults surrounded by an annulus of normal faults and regional normal faults surrounding the annulus. The surface loading with added stress caused central thrust faults to form straight lineaments parallel to the regional thrust faults that surround the annulus of normal faults.

Cyr and Melosh focused the majority of their hypothesis on the upwarp stage of the model. Their results showed that upwarping is applicable to diapirs and can create radial fractures on the central region of the corona. The two-stage model suggests that for a depression to occur in the central region of the corona there must be surface loading. Surface loading would cause a deposit of lava flows to cover the radial fractures.

Koch and Manga (1996) investigated the behavior of stress and the topographic features used to characterize coronae created from diapirs. The assumptions that Koch and Manga used in their model included: 1) cylindrical geometry; 2) layers were isotropic and homogeneous; 3) the diapir behaved like

a Newtonian fluid; 4) a Bousinesq-like approximation (states that the density differences are negligible, except when the acceleration due to gravity is involved); and 5) the phase transition (an abrupt change from one physical property into another due to a change in a thermodynamic variable, such as temperature) was $\Gamma = 0.8$ ($\Gamma = (\rho - \rho_c)/(\rho_m - \rho_c)$). These workers used defined densities of a gabbro-eclogite with the densities being $\rho_m > \rho > \rho_c$ (ρ_m = density of the mantle ($\sim 3.4 \text{ g/cm}^3$); ρ = density of the diapir ($\sim 3.3 \text{ g/cm}^3$); and ρ_c = density of the crust ($\sim 2.9 \text{ g/cm}^3$)). The model begins with a spherical diapir that has a radius (a), density (ρ), and viscosity ($\lambda\mu$) (Fig. 20). The diapir rises through a fluid half-space in the mantle with density ρ_m , and spreads laterally beneath the crustal layer with density ρ_c . The motion of the diapir and topography were calculated by the boundary integral method (Manga et al., 1993; Koch, 1994). The portion of the diapir below the level of neutral buoyancy (b) is defined as the positively buoyant side, whereas the portion of the diapir that infiltrates the level of neutral buoyancy is the negatively buoyant side. The possible radii and crustal thickness that the authors considered ranged from $0.05 < b/a < 0.5$ (b = crustal thickness, a = diapir radius). They assumed that the viscosity of the mantle is $\mu = 10^{21}$ Pascals, radius is $a = 100 \text{ km}$, and difference in density is $\rho_m - \rho = 100 \text{ kg/m}^3$.

The model enabled Koch and Manga to predict the surface features that would occur during the different developmental stages of the diapir with mathematical calculation and computer simulations. As the diapir rises into the crust, domal topography occurs. The deviatoric stress is great enough that radial

fractures will occur on the crest. Rims and concentric deformation occur as the diapir spreads along the level of neutral buoyancy. As spreading continues, the concentric deformation becomes more focused near the rim. The final stage has the central region becoming depressed below the surrounding surface area.

Koch and Manga (1996) determined that the evolution from domal corona to a corona with a central depression takes ~50 m.y.

All three models predicted in similar structures formed by diapirism. 1) The diapir rises from below and reaches the lithosphere layer, causing the surface to dome upward and radial fractures to form. 2) The diapir flattens and spreads along the base of the layer, and a topographic rim and/or rim structures may develop, consisting of concentric fractures which become more focused close to the rim as the diapir continues to spread below the layer. 3) The diapir continues to spread until the plateau cannot support itself, causing gravitational relaxation and a depression in the central region of the structure.

Withjack and Scheiner's (1982) model focused more on the regional strain patterns occur during the doming. These authors did not consider the later evolution of the dome, however the presence of radial fractures and possible concentric fractures surrounding the central region indicate that the dome might follow similar stages as discussed by Koch and Manga (1996). Withjack and Scheiner (1982) did not address the density, the rheology, or the evolution of the diapir in their model. Cyr and Melosh (1993) focused on the tectonic patterns that would form as a result of a two-stage model. Cyr and Melosh (1993) did not think that the upwarping stage would create a central depression, however the

presence of radial fractures and the concentric fractures surrounding the central region indicates that the dome might follow similar stages discussed by Koch and Manga (1996). Koch and Manga (1996) focused on the formation of the dome as it evolves to a corona with a depression and pointed out the same types of deformation; the central region contains radial fractures surrounded by concentric fractures, as the previous models discussed (Withjack and Schiener, 1982; Cyr and Melosh, 1993). Compared to the other models, Koch and Manga (1996) focused on the behavior of the diapir over time that leads to surface deformation. The Withjack and Scheiner (1982) model focused on one stage and the Cyr and Melosh (1993) model focused on coronae being formed by two stages, instead of the dome gradually changing due to the behavior of the diapir and not volcanic loading.

Evaluation of Diapir Hypothesis

Experimental, analytical and finite-element models for the formation of diapiric structures indicate a common sequence of events during layer impingement from below of a buoyant diapir. Radial fractures are common elements of diapiric structures, although radial structures might not develop depending on the regional stress field. Fractures may develop perpendicular to the orientation of the minimum principal compressive stress but in this case the resulting diapiric structure is elongate rather than circular (Withjack and Scheiner, 1982; Cyr and Melosh, 1993).

Circular lows are similar to the end product of coronae evolution. The corona develops a depression in its central region, and both circular lows and coronae would have a depression surrounded by concentric fractures. However, other morphological features used to describe coronae show that the formation of circular lows may be inconsistent with diapiric formation, given the lack of radial fractures. Circular lows appear to not have disturbed the surrounding area. Based on the model predictions (Withjack and Scheiner, 1982; Cyr and Melosh, 1993; Koch and Manga, 1996), diapiric emplacement would cause deformation to the surrounding area. The lack of radial fractures could be caused by volcanism, but the circular lows mapped did not contain much evidence of volcanic activity. Nonetheless, one might expect some evidence of radial fractures extending beyond the interior of the structure and past the concentric fractures and rim.

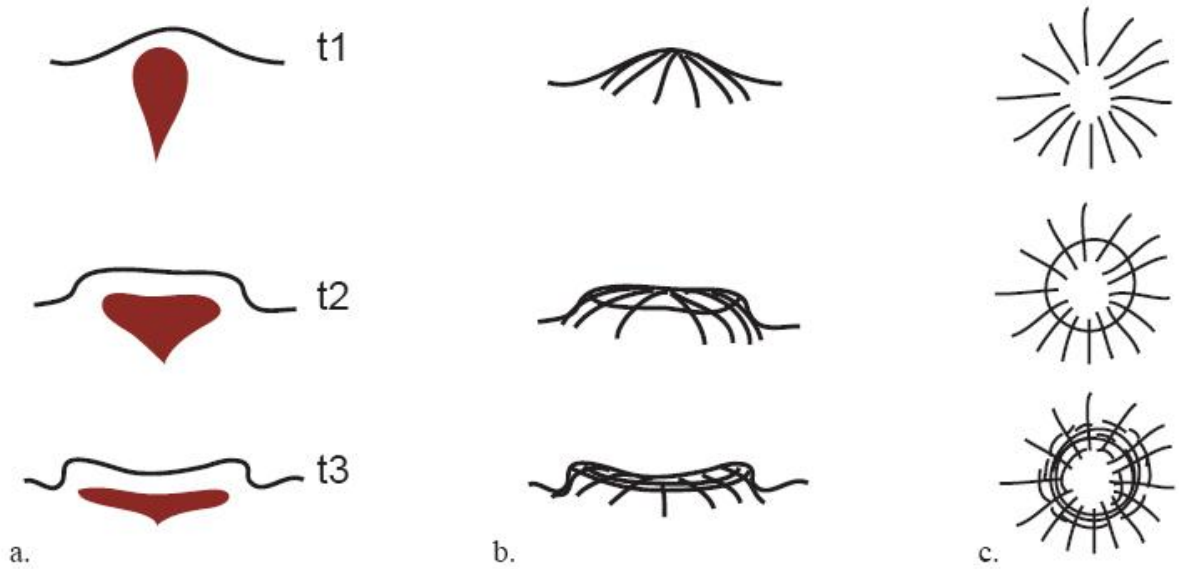


Figure 17. A generalized model of corona formation by diapiric rise: a) cartoon showing relation of diapir (red) and lithosphere. b) Side view of surface deformation caused by corona formation. c) Map view of surface deformation caused by corona formation. (After Koch and Manga, 1996) At t1, the mantle diapir rises, creating a dome-like feature. At t2, the diapir spreads beneath the lithosphere, flattening and changing from dome-like to plateau-like feature. At t3, the diapir cools, causing gravitational relaxation. (After Squyres et al., 1992)

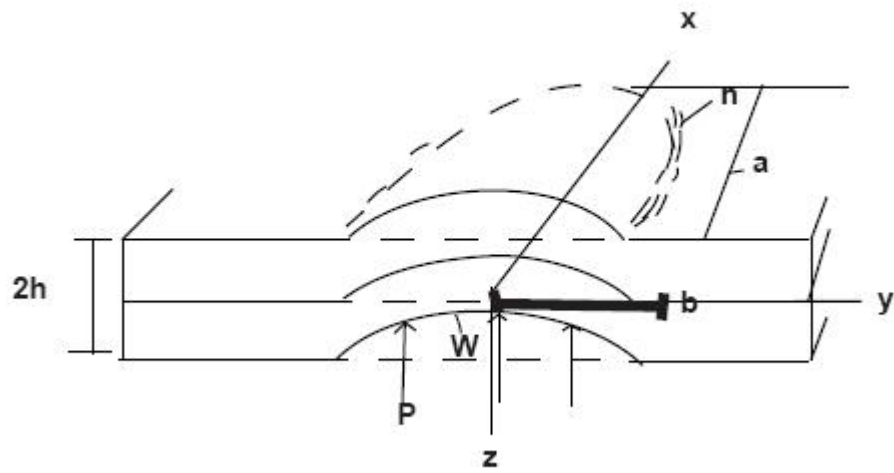


Figure 18. Model of doming in an x - y - z reference frame. The major and minor axes for the thick plate are a and b . The thickness of the plate is $2h$. The magnitude of the pressure beneath the plate is P , W is the vertical deflection, and n is the outward normal plate edge. (From Withjack and Scheiner, 1982)

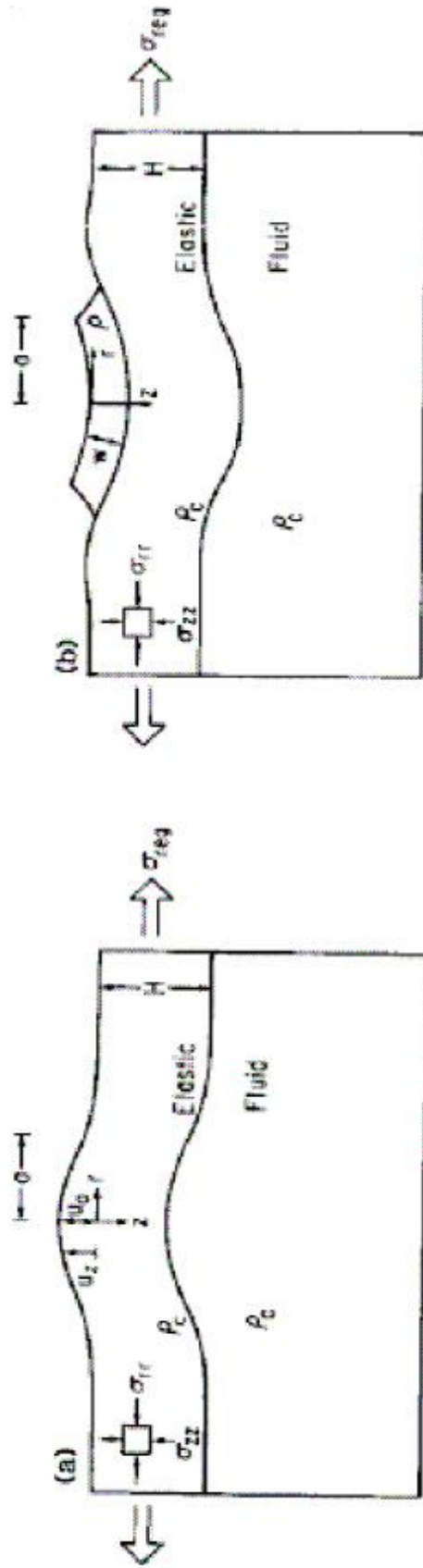


Figure 19. Two-stage model of corona formation. a) Upwarping is stage one for young corona causing it to dome by diapir. b) Surface loading is stage two for mature corona and causes a depression by volcanic material loading the area down. In both diagrams, H is the thickness of the lithosphere and ρ_c is the density. In (a), the depth below the surface is z , r is the radius of the corona center, u_0 is the amount of upwarp relative to the undeformed surface. In (b), the cylinder radius is a , the load thickness is w , and ρ is the corrected mantle density (From Cyr and Melosh, 1993).

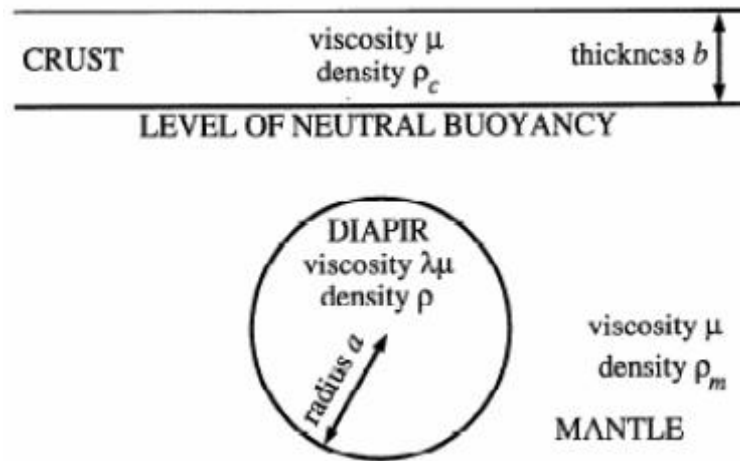


Figure 20. A diapiric model of corona formation. The diapir in its initial state with a diapir depth of $10a$ (Koch and Manga, after 1996)

Caldera Hypothesis:

Another endogenic process thought to form coronae are calderas (Janes et al., 1992; Squyres et al., 1992; Stofan et al., 1992; Stofan et al., 1997; DeLaughter and Jurdy, 1999). The definition of a caldera is a “crater or surface depression resulting from collapse of an underlying magma chamber roof during withdrawal of magma” (Carrigan, 2000). The diameter of calderas is based on the size of the collapsed magma chamber. The general characteristics used to identify calderas are: 1) topographic rim, 2) inner topographic wall, 3) possible bounding faults, and 4) caldera floor containing debris from caldera walls or flooding (Lipman, 2000). The topographic rim surrounds the caldera depression. For young calderas, the rim defines the size of the chamber, whereas old calderas may have an enlarged topographic rim and reduced topographic diameter due to erosion over time (Lipman, 2000). The inner topographic wall is concave, flattening down-slope creating an interior crater shape. Any bounding faults are nearly vertical to steeply-dipping and occur in the interior of the caldera. Bounding faults can also describe concentric fractures that occur from “gravitational slumping” of the caldera walls (Lipman, 2000). The caldera floor can contain debris from the collapsing walls or flooding may occur covering all the evidence of debris. Scientists have identified caldera-like structures on Venus’ surface. A typical caldera on Venus is identified by a circular to elongate shape, surrounded by an annulus of fractures along the topographic rim; the caldera floor is 1 to 3 km below the surrounding area and displays evidence of volcanic activity (Crumpler and Aubele, 2000). Calderas to caldera-like

structures with diameters ranging from 30 to 350 km on Venus are: arachnids, patera, and coronae (Fig. 21) (Barsukov et al., 1986; Head et al., 1992; Dawson and Crumpler, 1993; Stofan et al., 1992; Squyres et al., 1992; Janes et al., 1992; Crumpler et al., 1997; Stofan et al., 1997; DeLaughter and Jurdy, 1999; Crumpler and Aubele, 2000).

Coronae with depressions have been interpreted to originate as calderas (Barsukov et al., 1986; Stofan et al., 1992; Squyres et al., 1992; Janes et al., 1992; Stofan et al., 1997; DeLaughter and Jurdy, 1999). Squyres and colleagues (1992) identified these types of coronae as “circular depressions” due to their similarity to coronae characteristics used to identify coronae and calderas. The characteristics of “circular depressions” are simple topographic depressions with little or no rim (Squyres et al., 1992), consistent with the characteristics used to identify calderas. Squyres and colleagues (1992) only identified two coronae as circular depressions: Aramaiti and Thouris. Other scientists identified these structures as caldera-like and are interpreted as the end product of coronae evolution (Stofan and Head, 1990; Janes et al., 1992; Stofan et al., 1992; Koch, 1994; Stofan et al., 1997; DeLaughter and Jurdy, 1999). The caldera-like coronae are characterized by an annulus of fractures or ridges with a possible raised rim and annular “moat.” The interior of the caldera is deeper than the surrounding area and degraded lava flows surround the caldera (Stofan et al., 1992; Stofan et al., 1997; DeLaughter and Jurdy, 1999).

The difference between coronae originating from calderas and being caldera-like can be difficult to distinguish. Coronae originating from calderas

contain the same morphological characteristics as caldera-like coronae: annulus of concentric fractures or ridges with a depression and surrounded by volcanic flows (Barsukov et al., 1986; Stofan et al., 1992; Squyres et al., 1992; Janes et al., 1992; Stofan et al., 1997; DeLaughter and Jurdy, 1999). The collapsed magma chamber defines the size of a caldera diameter indicating that calderas can only be as big as their magma chamber. Calderas cannot be as large as coronae because of this size limit. The largest identified corona interpreted to have originate from a caldera is Aramaiti with the diameter of 350 km.

Evaluation of Caldera Hypothesis

A caldera is identified by a circular to elongate shape, surrounded by an annulus of fractures along the topographic rim, the caldera floor is 1 to 3 km below the surrounding area, and it contains evidence of volcanic flows (Crumpler and Aubele, 2000). Circular lows are similar to a caldera by being a circular structure surrounded by an annulus of fractures with a depression. The morphological characteristics of circular lows make them inconsistent with the caldera hypothesis. Previous works have identified Aramaiti and Thouris as possible calderas (Squyres et al., 1992; Stofan et al., 1992). Comparing these two circular lows to the characteristics used to identify calderas will illustrate that the formation of circular lows are inconsistent with this hypothesis. A Venusian caldera is 1 to 3 km below the surrounding area; in contrast, Aramaiti is only 0.1 to 0.2 km below the surrounding area (Fig. 14). Aramaiti has minor flooding on its northwest side (material unit E) and cuts tessera terrain on the northeast side

(Fig. 15). If Aramaiti was a caldera then there should be evidence of significantly more flooding and the depth of the caldera should be greater than 0.1 to 0.2 km as compared to Aramaiti's diameter. On the northwest edge of Aramaiti there is blocky material that is less than 20 km in size that could be debris or some other material. Thouris is not a caldera because it has a depth of 0.5 to 0.7 km compared to its 190 km diameter. If Thouris was a caldera then its depression should have a greater depth. Thouris cuts the suite of fractures and concentric fractures of the two coronae. If Thouris was a caldera then there should be flooding or debris in the interior or surrounding the structure to indicate that there was a collapse to form a caldera. Thouris' interior contains minor flooding caused by two small volcanoes located in the central region. The general difference between circular lows and calderas are circular lows are shallow depressions (less than or equal to 1 km) compared to their diameter size. They have minor flooding, but calderas should show major flooding as a result of magma chamber collapse. From the information gathered, circular lows are not consistent with the caldera hypothesis.

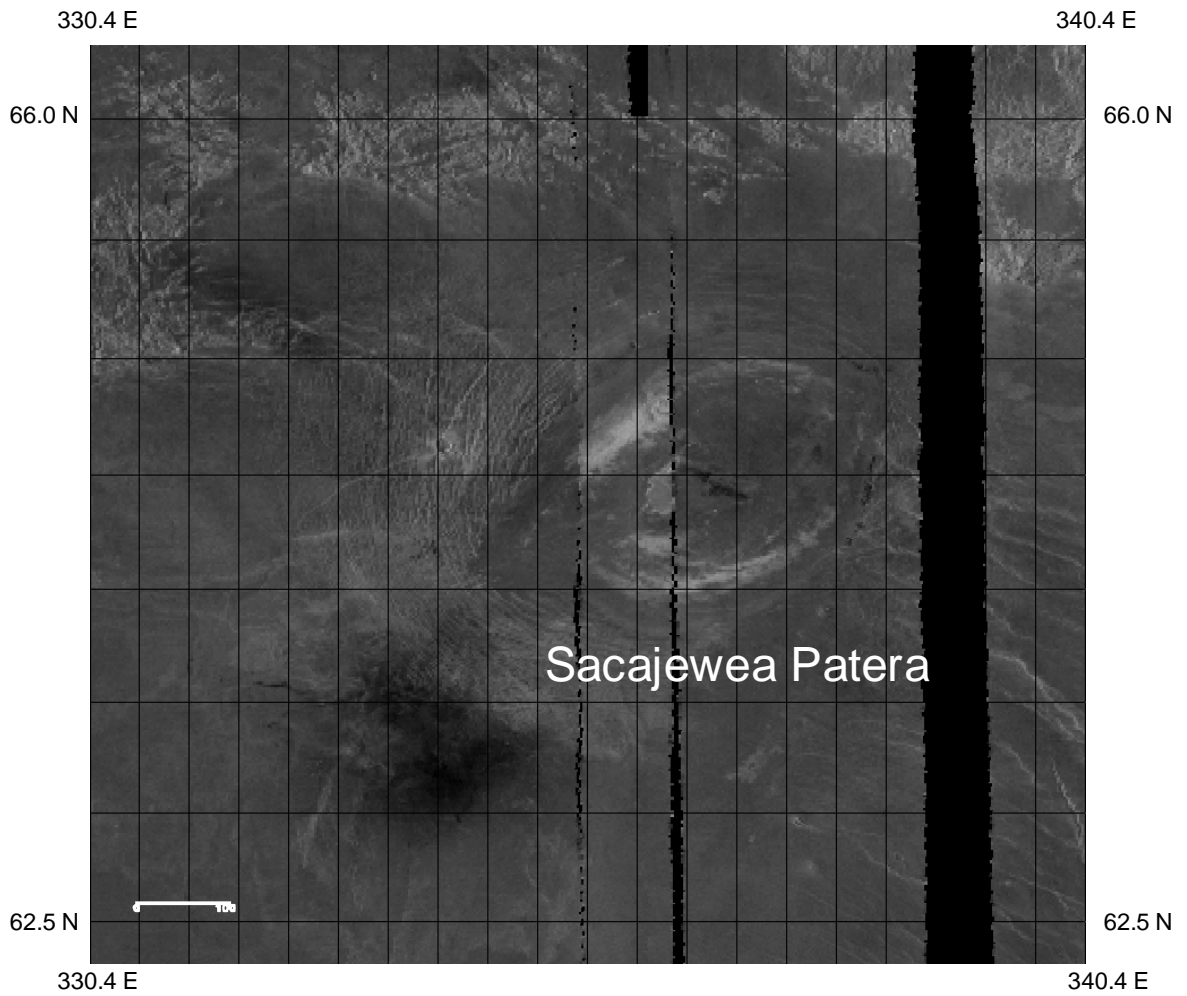


Figure 21. Left-illumination SAR image of Sacajewea Patera (64.3N/335.4E; 233.0 km diameter) is interpreted as a caldera. The radar-bright areas on Sacajewea Patera represent volcanic flows. The caldera has concentric fractures and a depression that is 2 km-deep. (Roberts and Head, 1990; Head et al., 1992)

Impact Crater Hypothesis:

Venus' hosts approximately 970 pristine impact craters that are distributed randomly across the planet with diameters ranging from about 1.5 to 270 km (Phillips et al., 1992; Schaber et al., 1992), overlapping the coronae diameters of about 60 to 2600 km. The general characteristics used to identify Venus' impact craters include circular depressions surrounded by sharp rims and radar rough ejecta. Structures identified as impact craters are generally pristine. Coronae have been interpreted as possible impact features that were modified after formation (Schaber and Boyce, 1977; Campbell et al., 1979; Campbell and Burns, 1980; Jurgens et al., 1980; Marsursky et al., 1980; Grieve and Head, 1981; Head and Solomon, 1981; Barsukov et al., 1986; Nikolayeva et al., 1986; Basilevsky, 1987; Squyres et al., 1992; Vita-Finzi, 2004; Hamilton, 2004).

Vita-Finzi and colleagues (2004) interpreted many coronae as impact craters. A log-normal frequency distribution was created using diameters of coronae and known impact craters to determine if coronae could be impact craters. Their results show that the median of impact craters smaller than coronae, however impact crater size distribution was similar to that of coronae. Their results indicate that larger coronae, with diameters greater than 1250 km, possibly originated from diapirs instead of bolide impacts because the larger coronae were considered statistical outliers. Ancient impact craters are modified structures. The processes that cause impact crater modification are: 1) endogenic processes, such as diapirism, 2) volcanism triggered by an impact, 3)

erosion over time; and 4) the behavior of the Venusian atmosphere over time (Greeley, 1987; Stewart et al., 1993; Anderson and Smrekar, 1999).

Hamilton (2004) interprets that all circular structures on Venus' surface are impact craters. Using the diameters of coronae, Hamilton used a log size/log distribution to determine that coronae size distribution is similar to impact craters. Hamilton points out that ancient impact craters have a degraded morphology due to surface processes such as sedimentation, wind, liquid, climate, atmosphere, and bolide effects. Tectonic and volcanic activity were also noted as other important processes that could change impact crater morphology.

Both Vita-Finzi and colleagues (2004) and Hamilton (2004) postulated that coronae might be ancient impact craters, but, Hamilton interpreted that all circular structures formed as impact craters. To determine whether coronae might be ancient impact craters, both parties used statistical methods. Hamilton described in detail the different variables that might cause coronae to have a different morphology than impact craters, where as Vita-Finzi and colleagues (2004) just mention possible variables.

Evaluation of Impact Crater Hypothesis

Vita-Finzi and colleagues (2004) and Hamilton (2004) interpreted surface process such as erosion as a major cause for ancient impact craters to become modified. To see whether or not circular lows could be ancient impact craters we can model the erosion of the pristine impact crater Mead and compare the final results to the circular lows. Mead (269 km diameter of outer rim; 194 km interior

diameter) is the largest exposed impact crater with a multiring basin similar in size to circular lows. The outer ring of Mead is 0.4 km above the surrounding area with a width of 40 km and the interior has a depth of 0.7 km below the surrounding area and 1.1 km below the outer ring (Herrick and Sharpton, 1996). Mead has a sharp contact around the structure with ejecta occurring around most of rim and surrounding the area. There are still remains of a halo surrounding the impact crater. A volcanic feature located northwest of Mead has its flows covering some of Mead's ejecta deposit (Fig. 22).

The rate of erosion on Venus is so small that it is negligible. I assumed that the dominant force to cause erosion was wind and had created the model based on that assumption. My results displayed that over time, the halo and ejecta would be the first materials to erode away. The sharp contact surrounding the structure would gradually disappear. The rim would decrease in height and possibly weather down to the height of the base. The debris from the rim could fill the depression and possibly make the rim wider on one side as it starts to weather. The fractures would not be as defined or would not be present if eroded. Concentric fractures could occur from gravitational slumping from rim walls (Fig. 22c). Circular lows are similar to the eroded Mead, by lacking a halo and ejecta. Mead and circular lows would have little to no rim. The shallow depression (less than or equal to 1 km) will be surrounded by concentric fractures. Mead and circular lows do not disturb their surrounding areas. The differences between circular lows and Mead are there appears to be no debris present in the interior or exterior of the circular lows with the exception of

Aramaiti. The sharp contact surrounding Mead would most likely disappear whereas the sharp contacts are still present on some of the circular lows, such as Zemlika. Four of the five circular lows cut tessera terrain that still has sharp contacts.

Three other impact craters were observed and compared to circular lows. All three impact craters were chosen because they impacted into tessera terrain (Fig. 23). The impact craters, Juliot-Curie (1.7S/62.4E; 100.9 km diameter), Andreianova (3.0S/69.0E; 69.5 km diameter), and de Beauvoir (2.0N/96.1E; 53.3 km diameter), do not appear to disturb or have caused any immediate deformation to their surrounding areas. It appears that the bolides impacted the surface modifying only the area they impacted. The circular lows do not appear to disturb their immediate area; they appear to behave in the same manner as the impact craters. Topographic profiles of the three impact craters appear similar to the topographic profiles of the circular lows. Impact crater de Beauvoir appears to be different than the circular low profiles, but this crater also has a different profile than the other two craters. Craters Juliot-Curie and Andreianova appear to have similar topographic profiles, each displaying an amphitheater-like shape. Even Mead has a similar topographic profile as the circular lows and the two similar impact craters. The depths of the impact craters range from 0.2 to 1.0 km, which is similar depth as the circular lows. The impact craters also have incomplete rims similar to the circular lows. Impact craters have some different characteristics than the mapped circular lows. They show ejecta adjacent to the impact, and are surrounded by a halo. Not all impact craters have halos and not

all impacts have very defined ejecta. This does not rule out circular lows as impact craters because haloes and ejecta could erode over time, and if these are ancient impact craters, then it is possible that the ejecta and haloes eroded. The sharp contacts occurring around the circular low could be interpreted as eroded ejecta. Aramaiti actually has some blocky unit material, material unit B, which could be interpreted as ejecta. The only problem with this is that the circular low is supposed to be a degraded impact crater, except the tessera terrain that it cuts appears to be in pristine condition – that is, not modified by significant erosion. The tessera should be as eroded, or more eroded, than the circular low. It is possible that the reason the tessera is not as eroded is rheology. The tessera terrain may have had a weaker rheology than its present rheology during the time of circular low formation. If the circular low formed during the time the tessera had a weaker rheology, it would explain why its physical characteristics have some differences with present impact craters.

Based on the information gathered from the mapping of circular lows and the information gathered from observing the impact craters Mead, Juliot-Curie, Andreianova, and de Beauvoir, the impact craters hypothesis appears to best fit the how the circular lows originated. Impact craters and circular lows have similar characteristics: 1) lack of radial fractures, 2) concentric fractures, 3) shallow amphitheater-like depression (less than or equal to 1 km), 4) lack of disturbance immediately surrounding the circular depression, 5) cookie-cutting truncation of the tessera terrain fabrics, and 6) rim. Even though de Beauvoir is

not as similar, its central region observed on the topographic profile can be interpreted as a dome, such as Aramaiti.

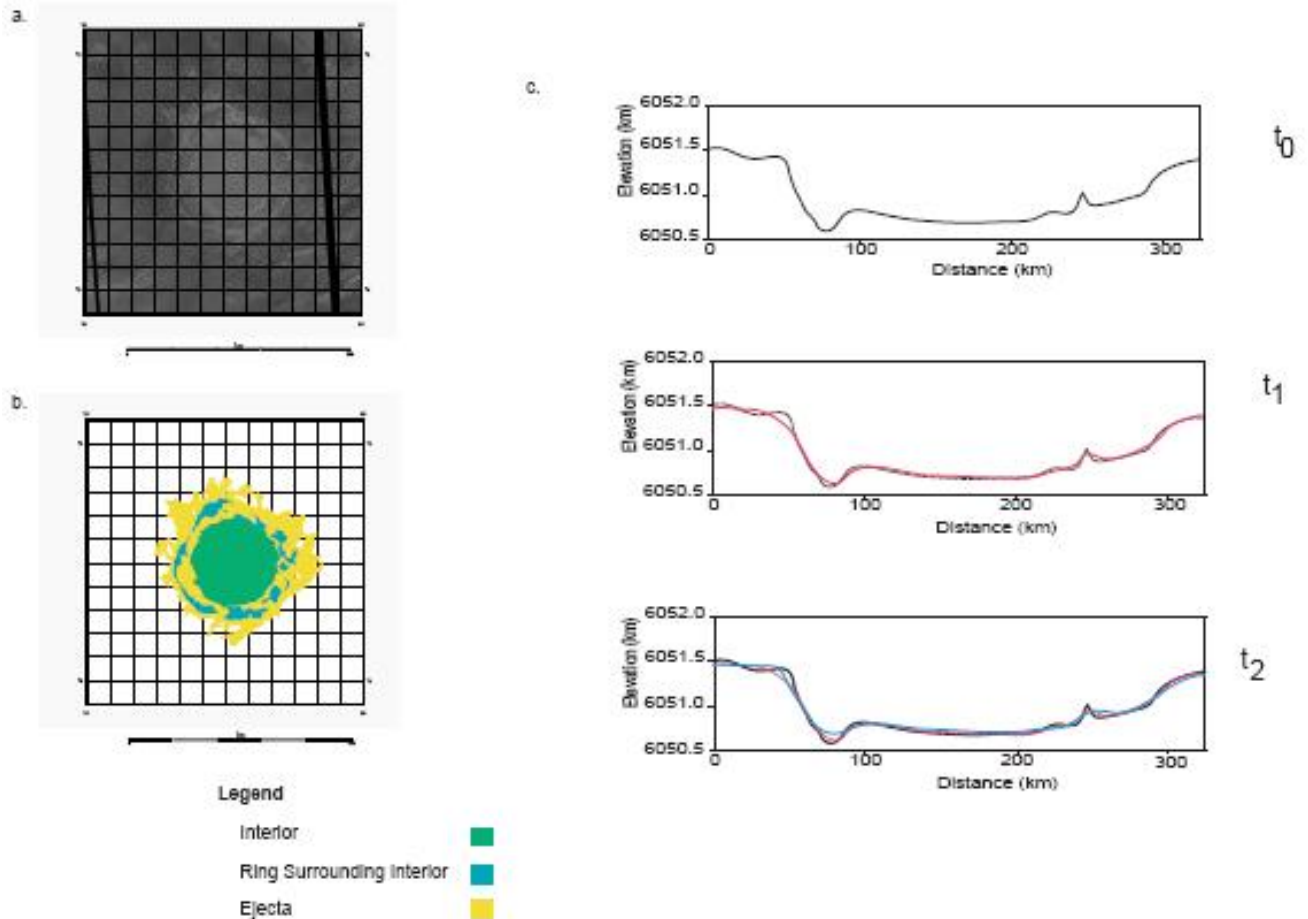


Figure 22. Mead impact crater (12.5N/57.2E) is the largest impact on Venus with a diameter of 269 km and 1 km depth. a) Left-illumination SAR image of Mead. b) Map of Mead highlighting the interior (green), ring surrounding interior (blue), and ejecta (yellow). c) Topographic profiles of showing how erosion might modifying the profile over time. At t_0 (black line), the impact is young and new. At t_1 (red line), the edges of the depression start to erode and fill in the depression. The tip of the peak gets rounded and sediment starts to fill on the side of the peak that is away from the depression. At t_2 (blue line), the edge of the depression gets more rounded and more sediment fills into the depression. The peak gets more rounded and more sediment fills on the side away from the rounded peak. The volume of sediment is preserved over time in this model.

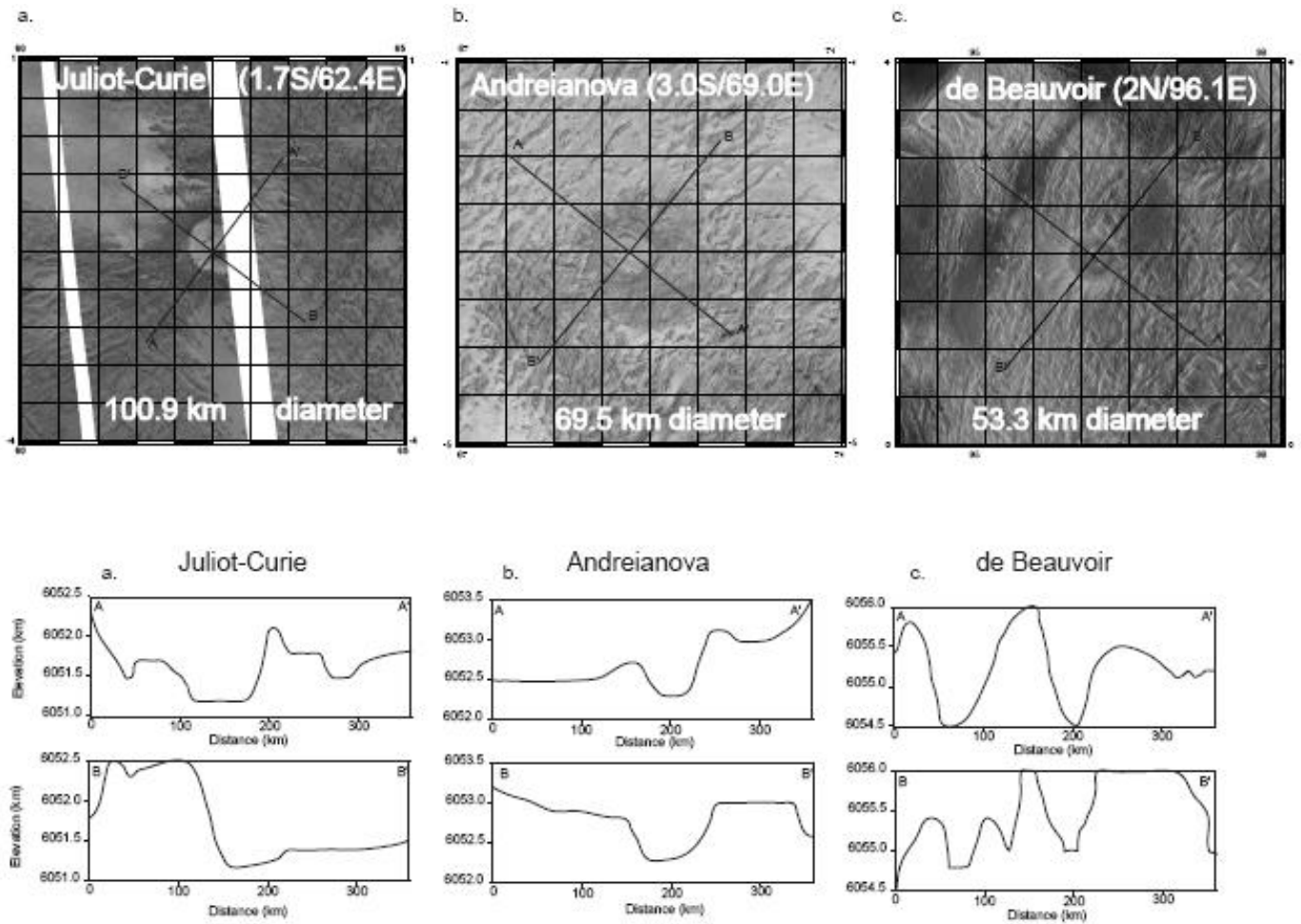


Figure 23. Left-illumination SAR and topographic profiles of three impact craters located in areas of tessera terrain: a) Juliot-Curie, b) Andreianova, and c) de Beauvoir.

Conclusion

The characteristics used to identify circular lows are circular to quasi-circular structures characterized by amphitheater-like depression with concentric fractures and a possible rim. The mapped circular lows appears inconsistent with the diapir and caldera hypotheses, indicating that it is possible for these circular lows to form from a different process. These circular lows appear to be more consistent with the characteristics of impact craters and could be possible impact craters. For a better understanding on whether these circular lows possibly represent ancient impact craters additional circular lows should be mapped and their geologic histories evaluated.

Implications

The implications that circular lows represent ancient impact craters would affect certain views about Venus, such as the widely held view that all coronae represent the surface expression of mantle diapirs on the lithosphere (Janes et al., 1992; Stofan et al., 1992; Squyres et al., 1992; Koch, 1994; Cyr and Melosh, 1993; Koch and Manga, 1996; Stofan et al., 1997; DeLaughter and Jurdy, 1999; Hansen, 2003), and the average model surface age on Venus (McKinnon et al., 1997). I identified approximately 50 circular lows that have been previously recognized as coronae. If these circular lows are impact craters, then re-analyzing the identified coronae and the criteria used to identify them would be important. This may narrow the list of characteristics used to identify coronae and may also reveal not all coronae identified were actually coronae.

If circular lows represent impact craters, then the relative surface age of Venus is older than what was previously calculated. Circular lows would affect the age because crater densities are used in the calculations (McKinnon et al., 1997). Even though there are about 50 identified circular lows, their diameters range from 60 to 380 km whereas the 970 identified impact craters range from 1.5 to 279 km (Phillips et al., 1992; Schaber et al., 1992, Herrick and Phillips, 1994; Herrick and Sharpton, 1996; Herrick et al., 1997; McKinnon et al., 1997). Most of the impact craters have a diameter less than 60 km, in contrast, most circular lows have a diameter greater than 100 km. Only 9 impact craters have diameters ranging from 100 to 269 km. There may be more impact craters than circular lows, but the densities make all the difference in the calculations and

circular lows have greater densities because they are larger. The circular lows would indicate that the planet is much older than was calculated. Further research would be needed to determine whether or not circular lows represent ancient impact craters.

APPENDIX

MAGELLAN DATA

The 1990 -1994 Magellan mission covered 98 percent of Venus collecting synthetic aperture radar (SAR), altimetry, gravity, and emissivity data. The Magellan satellite is a single instrument capable of collecting radar data in three different modes: synthetic aperture, radiometer, and altimeter mode (Ford et al., 1993). The SAR data operates at a wavelength of 12.6 cm with horizontal parallel transmit/receive polarization (HH), which allows the satellite to send pulses through the Venus' dense atmosphere to gather information from the planet's surface (Ford et al., 1993). Magellan's radar system used SAR, an antenna attached to the satellite that sends out pulses towards the planet's surface. The antenna moves through a collection of positions along its path as it is releasing and receiving pulses to create a radar image. The satellite travels in an elliptical orbit, which makes it necessary to vary the SAR imaging geometry and the viewing direction to be able to cover more surface area.

Appendix Table I. Characteristics of sensor and the orbit.

Parameter	<i>Value</i>
Radar system characteristics	
Wavelength, cm	12.6
Operating frequency, GHz	2.385
Modulation bandwidth, MHz	2.26
Transmitted pulse length, μ s	26.5
<i>SAR antenna</i>	
Gain dB	19.0
Angular bandwidth, deg	10 x 30
Polarization	HH

Effective slant-range resolution, m	88
Along track resolution, m	120
Orbit characteristics	
Periapsis altitude, km	289
Periapsis latitude, °N	9.5
Altitude at pole, km	2000
Inclination, deg	85.5
Period, hr	3.259
Repeat cycle, days	243

(From Ford et al., 1993)

SAR and altimetry data were used in my research. An altimeter determines the distance between the satellite and an area on the surface approximately 10 to 30 km in diameter (footprint – size of altimeter) (Plaut, 1993). The altimeter travels along and across tracks to produce a topographic map of the surface. The diameter of the altimeter footprint varies with latitude. SAR data can provide information for surface roughness, and orientation. SAR image brightness depends on the topographic effects, roughness, and electrical properties of the imaged surface (Ford and Plaut, 1993). A surface will appear bright if the surface roughness is at the scale of the radar wavelength. The surface will appear dark if the surface roughness is below the scale of radar wavelength. Topography influences the SAR data by collecting pulses from terrains sloping towards the satellite making the terrain appear bright on one side and dim on the other. Radar brightness is a function of surface roughness in relation to radar wavelength. If surface variation is near the size of the radar's wavelength it will cause strong backscattering. Electrical properties are difficult to deconvolve. Inverting the SAR image makes radar rough areas dark and radar smooth areas bright (Ford and Plaut, 1993). Inverted SAR is particularly useful for delineating structures because the human eye sees dark lines on bright surfaces more easily than the inverse.

SAR image interpretation can have some difficulties due to some problems with data collection. The satellite pulses energy of high elevation will return to the antennae before areas of low elevation. Foreshortening will occur causing the area of higher elevation to be imaged a position closer to the satellite than its actual position. An echo of a pulse from a high elevation returns before

the lower elevation in front of the high elevation, lay-over can occur, which the image is being on top of the base. Another problem to be aware of when dealing with SAR imaging is radar shadows. Radar shadows occur when the object is tilted away from the radar direction at an angle greater than the incident angle causing the object not to appear in the SAR image (Ford and Plaut, 1993). Using left-illumination, right-illumination, and stereo imagery of the same area can allow one to address these concerns.

References

- Anderson, F.S., and Smrekar, S.E. (1999) Tectonic effects of climate change on Venus. *Journal of Geophysical Research*. **104**, 30743-30756.
- Barsukov, V.L., and 29 others (1986) The geology and geomorphology of Venus from radar measurements by Venera 15 and 16 probes. *Journal of Geophysical Research*. **39**, 378-398.
- Basilevsky, V.L., Pronin, A.A., Ronca, L.B., Kryuchkov, V.P., Sukhanov, A.L., and M.S. Markov, M.S. (1986) Styles of tectonic deformation on Venus: Analysis of Veneras 15 and 16 data. *Journal of Geophysical Research*. **91**, 399-411.
- Basilevsky, A.T., Ivanov, B.A., Burba, G.A., Chernaya, L.M., Kryuchkov, V.P., Nikolaeva, O.V., Campbell, D.B. and Ronca, L.B. (1987) Impact craters of Venus: A continuation of the analysis of data from the Venera 15 and 16 spacecraft. *Journal of Geophysical Research*. **92**, 12869-12901.
- Campbell, D.B., Burns, B.A., and Boriakoff, V. (1979) Venus: Further evidence of impact cratering and tectonic activity from radar observations. *Science*. **204**, 1424-1427.
- Campbell, D.B., and Burns, B.A. (1980) Earth-based radar imagery of Venus. *Journal of Geophysical Research*. **85**, 8271-8281.
- Carrigan, C.R. (2000) Plumbing systems. Encyclopedia of Volcanoes. *in* Houghton, B., McNuthg, S.R., Rymer, H., and Stix, J., eds., *Encyclopedia of Volcanoes*. San Diego, Academic Press, p. 219-235.
- Crumpler, L.S., Aubele, J.C., Senke, D.A., Keddie, S.T., Magee, K.P., and Head, J.W. (1997) Volcanoes and centers of volcanism on Venus. *in* Bouger, S. W., Hunten, D. M., and Phillips, R. J., eds., *Venus II: Tucson*, University of Arizona Press, p. 697-756.
- Crumpler, L.S., and Aubele, J.C. (2000) Volcanism on Venus. Encyclopedia of Volcanoes. *in* Houghton, B., McNuthg, S.R., Rymer, H., and Stix, J., eds., *Encyclopedia of Volcanoes*. San Diego, Academic Press, p. 727-769.
- Cyr, K.E., and Melosh, H.J. (1993) Tectonic patterns and regional stresses near Venusian coronae. *Icarus*. **102**, 175-184.
- DeLaughter, J.E., and Jurdy, D.M. (1999) Corona classification by evolutionary stage. *Icarus*. **139**, 81-92.

- Ford, J.P. (1993) Chapter 1. Magellan: the mission and the system. *in* Ford, J.P., Plaut, J.J., Weitz, C.M., Farr, T.M., Senske, D.A., Stofan, E.R., Michaels, G., and Parker, T.J. eds., *Guide to Magellan Image Interpretation*: Pasadena, JPL Publication 93-24, p.1-5.
- Ford, J.P. and Plaut, J.J. (1993) Chapter 2. Magellan image data. *in* Ford, J.P., Plaut, J.J., Weitz, C.M., Farr, T.M., Senske, D.A., Stofan, E.R., Michaels, G., and Parker, T.J. eds., *Guide to Magellan Image Interpretation*: Pasadena, JPL Publication 93-24, p.7-18.
- Freeman, T. (1996) What is imaging radar? *JPL Imaging Radar Information*.
<http://southport.jpl.nasa.gov/>
- Greeley, R. (1987) *Planetary Landscapes*, 2nd ed., Allen & Unwin, London.
- Grieve, R.A.F., and Head, J.W. (1981) Impact cratering, a geological process on the planets. *Episodes*. **4**, 3-9.
- Hamilton, V.E., and Stofan, E.R. (1996) The geomorphology and evolution of Hecate Chasma, Venus. *Icarus*. **121**, 171-194.
- Hamilton, W.B. (2004) Plumeless Venus has ancient impact-accretionary surface. *in* Foulger, G.R., Anderson, D.L., Natland, J.H., and Presnall, D.C., eds. *Plates, Plumes, & Paradigms*, GSA, Special Papers (in Press).
- Hansen, V.L. and Willis, J.J. (1996) Structural analysis of a sampling of tesserae: implications for Venus geodynamics. *Icarus*. **123**, 296-312.
- Hansen, V.L., Willis, J.J., and Banerdt, W.B. (1997) Tectonic overview and synthesis. *in* Bouger, S. W., Hunten, D. M., and Phillips, R. J., eds., *Venus II*: Tucson, University of Arizona Press, p. 797-844.
- Hansen, V.L. and Willis, J.J. (1998) Ribbon terrain formation, southwestern Fortuna Tessera, Venus: implications for lithosphere evolution. *Icarus*. **139**, 116-136.
- Hansen, V.L. (2000) Geologic mapping of tectonic planets. *Earth and Planetary Science Letters*. **176**, 527-542.
- Hansen, V.L. (2003) Venus diapirs: Thermal or compositional. *GSA Bulletin*. **115**, 1040-1052.
- Hartmann, W.K. (1999) Chapter 9: Planetary surfaces I: petrology, primitive surfaces, and cratering. *Moons and Planets*. Belmont, Wadsworth Publishing Company, p. 249-258.

- Head, J.W., and Solomon, S.C. (1981) Tectonic evolution of the terrestrial planets. *Science*. **213**, 62-76.
- Head, J.W., Campbell, D.B., Elachi, C., Guest, J.E., McKenzie, D.P., Saunders, R.S., Schaber, G.G., and Schubert, G. (1991) Venus volcanism: initial analysis from Magellan data. *Science*. **252**, 276-288.
- Head, J.W., Crumpler, L.S., Aubele, Jayne, C., Guest, J.E., and Saunders, R.S. (1992) Venus volcanism: classification of volcanic features and structures, associations, and global distribution from Magellan data. *Journal of Geophysical Research*. **97**, 13153-13197.
- Herrick, R.R., and Phillips, R.J. (1994) Implications of a global survey on Venusian impact craters. *Icarus*. **111**, 387-416.
- Herrick, R.R., and Sharpton, V.L. (1996) Geologic History of Mead impact basin, Venus. *Geology*. **24**, 11-14.
- Herrick, R.R., Sharpton, V.L., Malin, M.C., Lyons, S.N., and Freely, K. (1997) Morphology and morphometry of impact craters. *in* Bouger, S. W., Hunten, D. M., and Phillips, R. J., eds., Venus II: Tucson, University of Arizona Press, p. 1015-1046.
- Herrick, R.R. and Sharpton, V.L. (2000) Implications from stereo-derived topography of Venusian impact craters. *Journal of Geophysical Research*. **105**, 20,245-20,262.
- Janes, D.M., Squyres, S.W., Bindschadler, D.L., Baer, G., Schubert, G., Sharpton, V.L., and Stofan, E.R. (1992) Geophysical models for the formation and evolution of coronae on Venus. *Journal of Geophysical Research*. **92**, 16055-16068.
- Janes, D.M., and Squyres, S.W. (1995) Viscoelastic relaxation of topographic highs on Venus to produce coronae. *Journal of Geophysical Research*. **100**, 21173-21187.
- Jurgens, R.F., Goldstein, R.M., Rumsey, H.R., and Green, R.R. (1980) Images of Venus by three-station radar interferometry – 1977 results. *Journal of Geophysical Research*. **85**, 8282-8294.
- Kirk, R.L., Soderblom, L.A., and Lee, E.M. (1992) Enhanced Visualization for Interpretation of Magellan Radar Data: Supplement to the Magellan Special Issue. *Journal Geophysical Research*. **97**, 16,371-16,380.
- Koch, D.M. (1994) A spreading drop model for plumes on Venus. *Journal of Geophysical Research*. **99**, 2035-2052.

- Koch, D.M., and Manga, M. (1996) Neutrally buoyant diapirs: a model for Venus coronae. *Geophysical Research Letters*. **23**, 225-228.
- Lipman, P.W. (2000) Calderas. Encyclopedia of Volcanoes. in Houghton, B., McNuthg, S.R., Rymer, H., and Stix, J., eds., *Encyclopedia of Volcanoes*. San Diego, Academic Press, p. 643-661.
- Manga, M., Stone, H.A., and O'Connell (1993) The interaction of plume heads with compositional discontinuities in the Earth's mantle. *Journal of Geophysical Research*. **98**, 19979-19990.
- Masursky, H., Eliason, E., Ford, P.G., McGill, G.E., Pettengill, G.H., Schaber, G.G. and Schubert, G. (1980) Pioneer Venus radar results: Geology from images and altimetry. *Journal of Geophysical Research*. **85**, 8232-8260.
- McKinnon, W.B., Zahnle, K.J., and Melosh, H.J. (1997) Cratering on Venus: models and observations. in Bouger, S. W., Hunten, D. M., and Phillips, R. J., eds., *Venus II*: Tucson, University of Arizona Press, p. 969-1014.
- Nikolayeva O.V., Ronca, L.B., and Basilevsky, A.T. (1986) Circular features on the plains of Venus as evidence of its geologic history. NASA TM-88566, Translation of "Krugovyye obrazovaniya na ravinakh Venery kak svideteli yeye geologicheskoy istorii," *Geokhimiya*. **5**, 579-589.
- Phillips, R.J., Raubertas, R.F., Arvidson, R.E., Sarkar, I.C., Herrick, R.R., Izenberg, Noam, and Grimm, R.E., (1992) Impact craters and Venus resurfacing history. *Journal Geophysical Research*. **97**, 15,923-15,948.
- Phillips, R.J. and Hansen, V.L. (1994) Tectonics and magmatic evolution of Venus. *Annual Review of Earth and Planetary Science*. **22**, 597-654.
- Plaut, J.J. (1993) Chapter 3. the non-SAR experiments. in Ford, J.P., Plaut, J.J, Weitz, C.M., Farr, T.M., Senske, D.A., Stofan, E.R., Michaels, G., and Parker, T.J. eds., *Guide to Magellan Image Interpretation*: Pasadena, JPL Publication 93-24, p.19-31.
- Pronin, A.A. and Stofan, E.R. (1990) Coronae on Venus: Morphology and distribution. *Icarus*. **87**, 452-474.
- Roberts, K.M., and Head, J.W. (1990) Western Ishtar Terra and Lakshmi Planum, Venus: models of formation and evolution. *Geophysical Research Letters*. **17**, 1341-1344.
- Saunders, R.S., and 26 others. (1992) Magellan Mission summary. *Journal of Geophysical Research*. **97**, 13,067-13,090.

- Schaber, G.G., and Boyce, J.M. (1977) Probable distribution of large impact basins on Venus – comparison with Mercury and the moon. *in* Roddy, D.J., Pepin, R.O., and Merrill, R.B., eds. *Impacts and explosion cratering – Planetary and terrestrial implications*. New York, Pergamon Press, p.603-612.
- Schaber, G.G., Strom, R.G., Moore, Soderblom, L.A., Kirk, R.L., Chadwick, D.J., Dawson, D.D., Gaddis, L.R., Boyce, J.M., and Russell, J. (1992) Geology and the distribution of impact craters on Venus: What are they telling us? *Journal of Geophysical Research*. **97**, 13,257-13,301.
- Smerkar, S.E., Kiefer, W.S., and Stofan, E.R. (1997) Large volcanic rises on Venus. *in* Bouger, S. W., Hunten, D. M., and Phillips, R. J., eds., *Venus II*: Tucson, University of Arizona Press, p. 845-878.
- Smerkar and Stofan (1997) Corona formation and heat loss on Venus by coupled upwelling and delamination. *Science*. **277**, 1280-1294.
- Smrekar, S.E., and Stofan, E.R. (1999) Origin of corona-dominated topographic rises on Venus. *Icarus*. **139**, 100-115.
- Stewart, C.A., Rampino, M.R., and Robinson, C. (1993) Impact shocks in the transition zone; enough energy to trigger a plume? Venus coronae linked to missing population of large Venus impact craters. *EOS, Transactions, AGU*. **74**, 80.
- Stofan, E.R., and Head, J.W. (1990) Coronae of Mnemosyne Regio, Venus: Morphology and origin. *Icarus*. **83**, 216-243.
- Stofan, E.R., Bindschadler, D.L., Head, J.W., and Parmentier, E.M. (1991) Corona Structures on Venus: Models of Origin. *Journal of Geophysical Research*. **96**, 20933-20946.
- Stofan, E.R., Sharpton, V.L., Schubert, G., Baer, G., Bindschadler, D.L., Janes, D.M., and Squyres, S.W. (1992) Global distribution and characteristics of coronae and related features on Venus: Implications for origin and relation to mantle processes. *Journal of Geophysical Research*. **97**, 13,347-13,378.
- Stofan, E.R., Hamilton, V.E., Janes, D.M., and Smrekar, S.E. (1997) Coronae on Venus: morphology and origin. *in* Bouger, S. W., Hunten, D. M., and Phillips, R. J., eds., *Venus II*: Tucson, University of Arizona Press, p. 931-965.

- Stofan, E.R., Smrekar, S.E., Tapper, S.W., Guest, J.E., and Grindrod, P.M. (2001) Preliminary analysis of an expanded corona database for Venus. *Geophysical Research Letters*. **28**, 4267-4270.
- Stofan, E.R., and Guest, J.E. (2003) Geologic Map of the Aino Planitia Quadrangle (V-46), Venus. Map. U.S. Geological Survey. Scale 1: 5 million. Geologic Investigations Series I-2779. (<http://pubs.usgs.gov/imap/i2779/>)
- Squyres, S.W., Janes, D.M., Baer, G., Bindschadler, D.L., Schubert, G., Sharpton, V.L., and E.R. Stofan. (1992) The morphology and evolution of coronae on Venus. *Journal of Geophysical Research*. **97**, 13,611-13,634.
- Vita-Finiz, C., Howarth, R.J., Tapper, S., and Robinson, C. (2004) Venusian craters and the origin of coronae. *LPSC XXXV*, Abstract **#1564**.
- Vita-Finiz, C., Howarth, R.J., Tapper, S., and Robinson, C. (2004) Venusian craters and the origin of coronae. http://www.mantleplumes.org/Venus_Craters.html. (extended version of abstract)
- Withjack, M., and C. Scheiner. (1982) Fault patterns associated with domes-an experimental and analytical study. *The American Association of Petroleum Geologists Bulletin*. **66**, 3002-316.